Original Article

Morphology and Formation of Crystalline Leucine Microparticles from a co-Solvent System using Multi-Orifice Monodisperse Spray Drying

Zheng Wang, Mani Ordoubadi, Hui Wang, Reinhard Vehring

Department of Mechanical Engineering, University of Alberta, Edmonton, Alberta, Canada

Abstract

The purpose of this study was twofold: to investigate leucine crystallization kinetics in co-solvent spray drying for a deeper understanding of the morphology and formation process of spray-dried crystalline particles, and also to develop multi-orifice plates using gallium focused ion beam milling in order to increase the production rate of monodisperse spray drying. A monodisperse spray drying technique using a vibrating orifice atomizer equipped with a gallium focused ion beam-manufactured dual-orifice plate was used to produce model particles in this study. The dual-orifice plate achieved an average production rate of 23.8 ± 2.0 mg/hr for the model particles, which allowed sufficient production of monodisperse powders for microscopic and spectroscopic analysis as well as fragility testing, within a reasonable spray drying time period. Leucine was dissolved in a water-ethanol co-solvent at ratios of 0.25/0.75 w/w, 0.5/0.5 w/w, and 1/0 w/w, and then spray dried at inlet temperatures of 20, 40, and 80 °C. Crystallinity of the spray-dried particles was confirmed by Raman spectroscopy. Numerical models were used to predict the crystallization and drying kinetics for the different co-solvent ratios and drying temperatures. Increasing the time available for crystallization correlated qualitatively with a larger crystal size. Changes in particle morphology affected the fragility of the particles, as illustrated in electron microscope images. This work highlights the importance of controlling crystal size and particle

morphology via solvent environment and drying temperature in the design and manufacture of microparticles for desired powder properties.

Introduction

Spray drying, a process to obtain dry powders by spraying liquid feeds into drying gas, is widely applied in the food (Shishir and Chen 2017; Tontul and Topuz 2017; Schmitz-Schug et al. 2016) and pharmaceutical (Ziaee et al. 2019; Arpagaus et al. 2018; Sosnik and Seremeta 2015) industries. Manufactured powders are often required to have specific properties for different applications. For example, efficient respiratory delivery requires particles sized within the respirable range (1-5 μm) (Mehanna et al. 2014), ideally with low-density and improved dispersibility (Vehring 2008), and with protection against moisture-induced deterioration in aerosolization performance (Li et al. 2016), etc. Although spray drying is a one-step process, particle formation during spray drying is complex and affected by many variables and processes. Therefore, in order to design target particles that can be readily manufactured, it is critical for particle engineering to draw on the necessary particle formation theory (Vehring 2008).

The liquid feed for spray drying can be in the form of a solution, emulsion, or suspension (Gharsallaoui et al. 2007). In solution-based spray drying, the droplet surface recedes quickly as the liquid droplets evaporate, promoting higher surface concentrations. Meanwhile, the solutes diffuse from the droplet surface towards the low-concentration core (Boraey and Vehring 2014). When the solute concentration at the droplet surface reaches the solubility limit, i.e. surface saturation, precipitation on the droplet surface can begin (Vehring 2008). For a crystallizing excipient, nucleation can commence when a specific level of supersaturation is reached, the value of which is a function of solvent composition and drying conditions. The time available for crystallization, which is considered as the time window for crystal nucleation, crystal growth, and polymorphic transformation, is an important parameter in crystallization kinetics since it can greatly influence the particle properties and morphologies (Ordoubadi et al. 2019; Baldelli et al. 2016). The

time available for crystallization is dependent on the initial feed concentration, initial droplet size, solubility, and evaporation rate. The initial feed concentration can be well controlled through careful feed preparation, and the initial droplet size is a known function of atomizer settings. However, the solubility and evaporation rate can change significantly, depending on the solvent environment.

A co-solvent system has frequently been used in spray drying to manipulate the solubility of pharmaceutical actives and excipients in order to obtain reasonable feed concentration (Boraey et al. 2013; Carr et al. 2011). Unlike the evaporation rate in a single solvent system, the evaporation rate in a co-solvent system can change (Ordoubadi et al. 2019). As a result, there can be great differences between the two types of systems in the time available for crystallization, leading to different crystallization kinetics and consequently different particle properties. The polymorphic forms of spray-dried particles can also be different in co-solvent systems, depending on the crystallization kinetics and the nature of the solvent system (Lee et al. 2011). Numerous studies have investigated the crystallization process of spray-dried particles. For instance, McDonagh investigated the crystallization of paracetamol particles spray dried from a water/ethanol co-solvent system and correlated the particle size, density, and morphology with the inlet temperature of the spray drying and the ethanol concentration of the feed (McDonagh and Tajber 2019). Lu investigated the droplet shrinkage, particle morphology, and polymorphic forms of mannitol particles spray-dried from an aqueous solution, correlating these characteristics with initial droplet size and feed concentration (Lu et al. 2020). Baldelli studied the influence of the crystallization process on the properties of sodium nitrate particles spray dried from an aqueous solution (Baldelli et al. 2016). The study found that longer time available for crystallization caused larger crystal size, higher crystallinity, a higher void fraction, and lower particle density. Ordoubadi developed numerical methods to study the evaporation kinetics and internal diffusion of multi-solvent droplets in spray drying for particle formation applications (Ordoubadi et al. 2019). In Ordoubadi's study, Leucine was spray dried from a water/ethanol co-solvent system at the same drying temperature (20 ℃) and different water/ethanol ratios (1/0, 0.75/0.25, 0.5/0.5, 0.25/0.75 w/w). The dimensionless values of the time available for crystallization were correlated with the initial ethanol mass

fraction. Different particle morphologies were observed and correlated with the initial ethanol mass fraction and the ethanol mass fraction at saturation. An interesting new morphology featuring a porous structure with crystals growing into the center of the particle was observed at the highest initial ethanol mass fraction. However, the precise details of crystallization kinetics in a co-solvent system, including crystal growth mechanisms and resulting crystal size and the correlation between crystallization kinetics and the time available for crystallization in a co-solvent system, require further investigation. Therefore, this study extends the previous work of (Ordoubadi et al. 2019) for a fundamental study of the morphology and formation of spray-dried crystalline leucine particles with an emphasis on crystal growth and particle formation mechanisms.

The time available for crystallization is very sensitive to the initial droplet size, which leads to additional complexity if the droplets are not uniform. As a result, crystallization kinetics and particle formation can be better studied in monodisperse model systems. The monodisperse droplet chain and monodisperse spray drying are two techniques commonly used to produce monodisperse droplets and dried particles. The monodisperse droplet chain uses a piezoceramic dispenser and produces monodisperse droplets when triggered by a pulse signal generated from a function generator. Droplets are injected into a heated airflow in a flow tube equipped with an imaging system for analysis of the initial droplet diameter. Dried particles are collected for characterization at the end of the flow tube using a membrane filter. A monodisperse droplet chain instrument has been discussed in detail elsewhere (Ordoubadi et al. 2019). Since monodisperse droplet chains produce droplets at each pulse signal, which is typically in the 100 Hz range, the production rates are much smaller than 1 mg/hr (Vehring et al. 2007). By contrast, monodisperse spray drying achieves a much higher production rate. Monodisperse spray drying systems consist of a monodisperse droplet generator and a spray dryer. Many different types of monodisperse droplet generators have been reported (Liu et al. 2015), and one type utilizing vibration forces generated by piezoelectric transducers has been commonly used in research studies (Rogers et al. 2012b, 2012a; Fu et al. 2011). A custom-designed vibrating orifice atomizer (Azhdarzadeh et al. 2016) integrated with a custom laboratory

spray dryer (Wang et al. 2019; Ivey et al. 2018) has been discussed previously in detail. In this system, the pressurized liquid feed formed a liquid jet through an orifice plate installed in the atomizer. The jet then disintegrated into monodisperse droplets under a specific frequency provided by a function generator. Compared with the monodisperse droplet chain dispenser, the vibrating orifice atomizer operated with a much higher vibration frequency in the 100-200 kHz range (Wang et al. 2019). As a result, monodisperse spray drying is able to produce over a thousand times more droplets, and consequently more final product, than the monodisperse droplet chain within the same time. However, the production rate of monodisperse spray drying is still not sufficient for the sample requirements of many typical powder assays. Thus, increasing the powder production rate of monodisperse spray drying becomes important and beneficial for particle design and characterization in research studies.

Certain multi-orifice designs have previously been shown to increase the production rate of monodisperse spray drying (Wu et al. 2007). Patel and Chen proposed a design of multiple ink-jet devices (Patel and Chen 2007) that can be grouped and mounted on the same plate to produce monodisperse droplets simultaneously. Each ink-jet device can be placed in an individual nozzle and supplied with liquid feed using individual tubing. However, this design of multiple ink-jet devices is not compatible with the custom spray dryer currently in use in our lab (Wang et al. 2019), and the re-design and re-manufacturing of the hardware is very time-consuming. Brenn designed a 62-hole plate to produce 62 liquid jets simultaneously and used laser drilling for manufacturing (Brenn et al. 1996). A liquid throughput up to 13.7 L/h was achieved using this nozzle plate. The diameter of the laser drilled holes was 63 μm, with 400 μm between adjacent holes. The droplet size ranged from 123 μm to 181 μm depending on the working frequency, and the monodispersity of the droplets was confirmed by visual observation. This multi-orifice design is compatible with the custom vibrating orifice atomizer currently in use in our lab (Wang et al. 2019); however, using laser drilling to manufacture micro-orifices carries some technical limitations. The orifices manufactured by laser drilling have been shown to have rough and irregular edges (Brenn et al. 1996) that can change the geometry of the orifice, thereby affecting performance; they can also make the orifice difficult to reproduce.

This problem of rough and irregular edges becomes more significant for smaller orifices, greatly limiting the use of laser drilling in the manufacture of very small orifices. Moreover, for a multi-orifice plate, in which each orifice should ideally be identical in order to produce monodisperse droplets, the rough and irregular edges can negatively influence the uniformity of the orifices and consequently the monodispersity of the produced droplets. By contrast, the technique of gallium focused ion beam (Ga-FIB) milling is capable of patterning and machining on a sub-micron level, thus allowing for higher resolution fabrication than laser drilling. This fact provided another motivation of this study, which was to develop custom multi-orifice plates with cleaner orifice edges and smaller orifice sizes using Ga-FIB milling.

The primary aim of this study was to investigate the crystallization kinetics of crystalline particles spray dried from a co-solvent system using monodisperse spray drying in order to acquire a deeper understanding of particle morphology and the particle formation process. In addition, given the low production rate of monodisperse spray drying, this study also aimed to develop multi-orifice plates in order to increase the production rate by using Ga-FIB milling for cleaner orifice edges and smaller orifice sizes than those in commercial laser-drilled orifice plates. Since this study also aimed for the fragility testing of the spray-dried particles, it was necessary to produce and collect sufficient powders from the cyclone. Increasing the production rate of monodisperse spray drying was, therefore, a necessary component of this study investigating the performance of crystalline leucine particles. Ga-FIB milling was used to manufacture the orifices on a thin stainless-steel plate, and scanning electron microscopy was used to observe the orifice edges. A custom vibrating orifice atomizer and custom laboratory spray dryer (Wang et al. 2019) were used to produce monodisperse particles. Leucine was selected as the crystallizing excipient since it was found to form fully crystalline particles from spray drying when it was the only solute (Feng et al. 2011; Lucas et al. 1999). Water/ethanol was selected as the co-solvent, not only because its use is common but, more importantly, because clear morphological differences in spray-dried leucine particles produced by a water/ethanol system as compared to an aqueous system (Ordoubadi et al. 2019) required further investigation. Leucine was dissolved in a water/ethanol co-solvent at different water/ethanol ratios and

spray dried at different inlet temperatures. Numerical methods in previous work (Ordoubadi et al. 2019) were used to predict the droplet evaporation rate, internal solute transfer, and other droplet drying kinetics in the co-solvent spray drying. The crystallinity of the spray-dried leucine particles was confirmed using Raman spectroscopy, and the particle morphology was analyzed using scanning electron microscopy.

Materials and Methods

Materials

L-Leucine (Cat. No. BP385-100, Acros Organics BVBA, Geel, Belgium) was dissolved in demineralized water and ethanol to prepare the feed solutions for monodisperse spray drying. Two different water/ethanol ratios, 0.25:0.75 w/w water/ethanol and 0.5:0.5 w/w water/ethanol, were chosen for this study and compared with a control system of 100% water. The feed solution concentration of leucine, 0.5 mg/mL, was the same for all formulations. The co-solvent ratios and feed solution concentration were chosen because clear morphological differences were reported previously using these parameters (Ordoubadi et al. 2019), and this study aimed for further investigation of the reasons for these differences.

Monodisperse Spray Drying using a Dual-Orifice Plate

The monodisperse spray drying setup used in this study has been discussed previously in detail (Ivey et al. 2018). Briefly, a vibrating orifice atomizer was supplied with pressurized feed solution to generate monodisperse droplets. A dual-orifice plate with two 30-µm-diameter orifices was installed in the atomizer to form two separate liquid jets. A piezoelectric ceramic ring attached to the atomizer head was actuated by a function generator to vibrate at a certain frequency. Control of the jet exit velocity through the pressure difference across the orifice and the driving frequency achieved an optimal monodisperse droplet disintegration in the Rayleigh jet disintegration regime, whereby the liquid jet disintegrates regularly into droplets of very similar diameter (Azhdarzadeh et al. 2016; Dumouchel 2008). Dispersing air was used to

disperse the droplets in a turbulent gas jet in order to minimize droplet collisions. The tendency for droplet collisions increases as the distance between droplets decreases; therefore the distance between droplets should be maximized (Brenn et al. 1997). One method of achieving such maximized droplet distance is to use air to disperse the newly formed droplets right after disintegration from the liquid column. A droplet dispersion system was designed previously for this purpose (Liu et al. 2011). In this study a similar design was used in which air flows through a dispersing cap integrated with the atomizer and disperses the droplets, thus reducing the droplet collisions and maintaining the monodispersity of the spray-dried particles. A schematic of the vibrating orifice atomizer using a dual-orifice plate is shown in Figure 1. The inlet drying gas temperature was set to 20 °C, 40 °C and 80 °C for different formulations. The droplets were then dried into solid particles in a custom lab-scale spray dryer (Ivey et al. 2018) and collected in a glass bottle using a stainless-steel cyclone separator. The cyclone had a cylinder-on-cone design with a tangential inlet. The drying gas flow rate was set to 0.5 m^3/min to ensure efficient collection of particles larger than 1 μm. The heat loss to surroundings generally depended on the inlet temperature, outlet temperature, and the Reynolds number in the drying chamber. From previous characterization experiments (Ivey 2018), the heat loss at a 0.5 m^3/min drying gas flow rate and inlet temperatures of 20 °C, 40 °C and 80 °C was determined to be around 0 kW, 0.06 kW and 0.22 kW, respectively. The liquid throughput was measured gravimetrically by using a small glass vial to collect the water flowing through the orifices in a time span of 2 min. Table 1 lists the detailed spray drying parameters. Table 2 lists all the formulations that were spray dried in this study.

Figure 1

Table 1

Table 2

Powder Production Rate

The powder production rate for monodisperse spray drying using a single-orifice plate, $\dot{m}_s$, was estimated as (Ivey et al. 2018)

$$\dot{m}_s = c_s Q = c_s C_d \frac{\pi d_o^2}{4} \sqrt{\frac{2\Delta p}{\rho_l}} \quad (1)$$

where c_s is the solids concentration of the feed solution, C_d is the discharge coefficient of the orifice, d_o is the orifice diameter (assuming a circular orifice), Δp is the pressure difference across the orifice and ρ_l is the liquid density. The discharge coefficient, C_d, is defined as the ratio of the actual or experimental flow rate to the theoretical flow rate. The discharge coefficient does not change significantly during atomization (assuming no clogging occurs) and varies only with different orifice geometry (Bayvel and Orzechowski 1993); thus it can be considered close to a constant for orifices with the same geometry. For example, the discharge coefficient is typically in the range of 0.7-0.8 for the circular orifice used in the vibrating orifice atomizer.

As shown in equation (1), the powder production rate is a function of three parameters: the solids concentration of the feed solution, the orifice diameter, and the pressure difference across the orifice. However, for applications in respiratory drug delivery, particles with a specific aerodynamic diameter, d_a, are required, which is not explicitly expressed in the equation. Therefore, equation (1) was rearranged into a function containing d_a as follows:

The solids concentration of the feed solution is related by (Vehring 2008) to the aerodynamic diameter of the spray-dried particle and the droplet diameter, d_D:

$$d_a = \left(\frac{\rho_P}{\rho_0}\right)^{\frac{1}{6}} \left(\frac{c_s}{\rho_0}\right)^{\frac{1}{3}} d_D \quad (2)$$

Here ρ_P is the particle density and ρ_0 is the unit density, 1 g/cm^3. The droplet diameter is related to the jet diameter, d_j, by (Rayleigh 1878):

$$d_D = 1.89 d_j = 1.89 d_o \quad (3)$$

This equation assumes that the vibrating orifice is operated with the optimal disturbance frequency and that the jet diameter is equivalent to the orifice diameter.

Equations (2) and (3) together give a relationship between d_a, c_s, and d_o which is

$$d_{\mathrm{a}} = 1.89\left(\frac{\rho_{\mathrm{P}}}{\rho_0}\right)^{\frac{1}{6}}\left(\frac{c_{\mathrm{s}}}{\rho_0}\right)^{\frac{1}{3}} d_{\mathrm{o}} \tag{4}$$

The powder production rate using a multi-orifice plate is proportional to the number of orifices, *N*, since multiple liquid jets are produced simultaneously.

By combining equations (1) and (4), the powder production rate using a multi-orifice plate can be expressed as

$$\dot{m}_{\mathrm{s},N} = 0.165 C_{\mathrm{d}} N \frac{d_{\mathrm{a}}^3}{d_{\mathrm{o}}}\sqrt{\frac{\rho_0^3}{\rho_{\mathrm{l}}\rho_{\mathrm{P}}}\Delta p} \tag{5}$$

For respiratory drug delivery, a specific target aerodynamic diameter of the particle is required in the range of 1-5 μm (Mehanna et al. 2014). From equation (5), the powder production rate for a given aerodynamic diameter of the spray-dried particle can only be increased by increasing the pressure difference across the orifice, decreasing the orifice diameter, and increasing the number of orifices. The pressure difference across the orifice is limited by the mechanical strength of the orifice plate in order to avoid rupturing the orifice. In addition, monodisperse droplet generation relies on the Rayleigh disintegration regime (Azhdarzadeh et al. 2016; Dumouchel 2008), which places an upper limit on the jet exit velocity. The jet exit velocity is related to the pressure difference across the orifice, which also carries an upper limit in order to ensure monodisperse droplet generation. Decreasing the orifice diameter is another option to increase the powder production rate, and small orifices are desirable to produce respirable particles. Typical feed concentrations in spray drying of respirable products are limited to the range of 10-100 mg/mL, due to the solubility limitations of the actives and excipients. The aerodynamic diameter of respirable particles is limited to the range of 1-5 μm. Thus, from equation (4), the ideal orifice diameter in this case is in the range of 1-10 μm. However, as previously mentioned, it is difficult to manufacture orifices in this size range with clean orifice edges and good reproducibility (especially at the lower end) by using laser drilling. As a result, Ga-FIB milling was investigated to manufacture small orifices in this study. The last and also the best way to increase the powder production rate is to increase the number of the orifices. Multi-orifice plates can only work ideally if each orifice is identical to ensure monodisperse droplet generation. Again, laser drilling

has its limitations in manufacturing uniform orifices, and Ga-FIB milling was investigated to manufacture multi-orifice plates.

Ga-FIB milling (Zeiss Orion HiM w/ Ga-FIB, Zeiss, Jena, Germany) was used to manufacture orifices on a 13-μm-thick circular stainless-steel plate. The aperture size of the Ga-FIB was 500 μm and the current was 30 nA. Dwell time was 5 μs. The node style was mitered, and the alignment was outside/in. These equipment parameters were chosen to optimize the manufacturing quality while keeping the manufacturing time within a reasonable range. Using these parameters, the average milling time for one 30-μm orifice was around 25 min. Ideally, more orifices are preferred on the plate, but due to the rather long operation time and high cost of the equipment the dual-orifice plate was manufactured in the early stage of this study and used to produce the model particles. The orifice diameter was 30 μm and the distance between the two orifices was around 200 μm. This is two times larger than the minimum distance between orifices reported by (Brenn et al. 1996) as necessary to ensure separate liquid jets, which is around three times the orifice diameter.

Numerical Model for Droplet Evaporation and Diffusion Kinetics

Determining the droplet evaporation and diffusion kinetics during spray drying is a complicated mass and heat transfer problem, especially for the multi-solvent system. Numerical methods to predict the droplet evaporation rate and internal solute transfer in the multi-solvent system have previously been discussed in detail (Ordoubadi et al. 2019). In this study, numerical methods utilizing the Stefan-Fuchs model in conjunction with Fick's law of diffusion were used to calculate droplet evaporation and diffusion kinetics and to determine leucine concentration profiles inside the evaporating droplets. In modeling the evaporation of a single droplet, the Maxwell model neglects the radial convective fluxes around the droplet, while the Stefan-Fuchs model takes these radial convective fluxes into consideration, giving more accurate results at higher temperatures; therefore, the latter model was chosen for this study. To model the internal diffusion

of the solute, Fick's law of diffusion was used. The numerical model is based on a well-mixed approximation which assumes the solvent compositions and temperatures are constant throughout the droplet, since the mass diffusivity of a molecule such as leucine is at least one order of magnitude larger than the mass diffusivity (and also the heat diffusivity) of ethanol and water. The numerical model also assumes zero partial pressure of the vapor in the drying gas. It is worth noting that the model is valid only up to the point of crystallization. With these assumptions, the generated numerical data agreed with the experimental data with only small differences (Ordoubadi et al. 2019). As a summary, the total evaporation rate of multi-solvent droplets, $\dot{m}_t$, was calculated from

$$\dot{m}_t = -2\pi d \rho_{\mathrm{t}} D_{\mathrm{g,m}} \ln\left(\frac{y_{\infty,\mathrm{g}}}{y_{\mathrm{s,g}}}\right) \tag{6}$$

in which d is the droplet diameter, ρ_{t} is the total gas density around the droplet, and $D_{\mathrm{g,m}}$ is the diffusion coefficient of the inert gas in the vapor mixture. $y_{\infty,\mathrm{g}}$ and $y_{\mathrm{s,g}}$ are the inert gas mass fractions under ambient conditions and near the droplet surface, respectively. The evaporation rate of each component, $\dot{m}_i$, was then calculated as

$$\dot{m}_i = \dot{m}_t \frac{y_{\infty,i}\beta_i - y_{\mathrm{s},i}}{\beta_i - 1} \tag{7}$$

where $y_{\infty,i}$ and $y_{\mathrm{s},i}$ are the vapor mass fractions of each component under ambient conditions and near the droplet surface, respectively; β_i can be approximated as $\left(\frac{y_{\mathrm{s,g}}}{y_{\infty,\mathrm{g}}}\right)^{\frac{D_{\mathrm{g,m}}}{D_{i,\mathrm{m}}}}$. Here $D_{i,\mathrm{m}}$ is the diffusion coefficient of each component in the vapor and gas mixture around the droplet.

Based on the total evaporation rate and the density of the liquid mixture, the diameter of the droplet was updated at each instance and the evaporation rate of the droplet was calculated from

$$\kappa = -\frac{\mathrm{d}d^2}{\mathrm{d}t} \tag{8}$$

The following modified Fick's law of diffusion for the inside of an evaporating droplet was then solved in conjunction with the appropriate boundary and initial conditions (Ordoubadi et al. 2019):

$$\frac{\partial C_j}{\partial t} = \frac{4D_j}{d^2}\left(\frac{\partial^2 C_j}{\partial R^2} + \frac{2\partial C_j}{R\,\partial R}\right) - \frac{\kappa R\,\partial C_j}{2d^2\,\partial R} \tag{9}$$

Here R is the radial coordinate non-dimensionalized by the instantaneous droplet radius, C_j is the concentration of each solute at each radial location and D_j is the diffusion coefficient of each solute inside the droplet. For the water/ethanol co-solvent system, D_j can be approximated by

$$D_j\sqrt{\eta_{\mathrm{m}}} = x_{\mathrm{l,w}}D_{j,\mathrm{w}}\sqrt{\eta_{\mathrm{l,w}}} + x_{\mathrm{l,eth}}D_{j,\mathrm{eth}}\sqrt{\eta_{\mathrm{l,eth}}} \tag{10}$$

where η_{m}, $\eta_{\mathrm{l,w}}$ and $\eta_{\mathrm{l,eth}}$ are the liquid viscosities of the mixture, water, and ethanol at the droplet temperature, respectively; $x_{\mathrm{l,w}}$ and $x_{\mathrm{l,eth}}$ are the mole fractions of water and ethanol in the droplet, respectively; and $D_{j,\mathrm{w}}$ and $D_{j,\mathrm{eth}}$ are the diffusion coefficients of solute j in water and ethanol, respectively. This equation also captures the fact that the diffusion coefficient of each solute in the mixture depends not only on the solvent composition, but also on the droplet temperature, which is affected by the drying temperature.

The surface concentration of each solute was then compared to the solubility of the solute at the respective solvent composition to find the appropriate particle formation parameters, such as the available time for crystallization.

Time Available for Crystallization

An important parameter in predicting the crystallization kinetics during spray drying is the time available for crystallization, t_{c}, which is defined as (Ordoubadi et al. 2019; Baldelli et al. 2016)

$$t_{\mathrm{c}} = t_{\mathrm{D}} - t_{\mathrm{s}} \tag{11}$$

where t_D is the total lifetime of the droplet and t_s is the time for the solute to reach saturation. The time available for crystallization can be considered as the time window available for nucleation and crystal growth. As the droplet shrinks during evaporation, the solute concentration increases on the droplet surface, generally faster than inside the droplet (Vehring 2008; Vehring et al. 2007), and reaches saturation there first, causing crystallization to start at the surface. Thus, in this study t_s is defined as the time from atomization to the point where the surface saturation of leucine reaches 1. However, nucleation may not happen instantaneously when the surface saturation reaches 1, and a certain level of supersaturation is usually required to trigger nucleation (Baldelli and Vehring 2016). Therefore, an additional time point, namely the time to reach critical supersaturation at which the nucleation can commence instantaneously, is also important in determining the time available for crystallization (Ordoubadi et al. 2020). Based on the time to reach critical supersaturation, the time available for crystallization can be determined by

$$t_c^* = t_D - t_n \tag{12}$$

where t_n represents the time to reach critical supersaturation. To determine this time point, the value of critical supersaturation, S_n, must be obtained first. He et al. proposed a model based on an evaporating droplet crystallization platform to predict the critical supersaturation at which nucleation can commence instantaneously (He et al. 2006). Based on the model, the critical supersaturation can be approximated by solving the following equation

$$\ln^3 S_{n,i} + \left[\ln\left(A_i/J_{n,i}\right)\right]\left[\ln^2 S_{n,i}\right] - B_i = 0 \tag{13}$$

where A_i is the diffusion-limited nucleation rate, $J_{n,i}$ is the nucleation rate at the point of critical supersaturation, and B_i is the thermodynamic parameter, defined as

$$B = \frac{16\pi v_{m,i}^2 \sigma_i^3}{3(kT)^3} \tag{14}$$

where $v_{m,i}$ is the volume of the solute molecule, σ is the surface energy of the solute in the solution, k is the Boltzmann constant, and T is the solution temperature in Kelvins. As noted in (He et al. 2006), the

surface energy has a strong correlation with the solubility $C_{\mathrm{sol},i}$; thus the following correlation was used (Christoffersen et al. 1991)

$$\frac{\sigma_i d_{\mathrm{m},i}^2}{kT} = \frac{1}{\pi}\ln\left(\frac{\rho_i}{\gamma_{\mathrm{sol},i} C_{\mathrm{sol},i}}\right) \tag{15}$$

where $d_{\mathrm{m},i}$ is the molecular diameter calculated using the molecule volume, ρ_i is the crystal density, and $\gamma_{\mathrm{sol},i}$ is the activity coefficient of the solvent in the presence of the solute molecules at saturation. With the assumption of spherical molecules ($v_{\mathrm{m},i} = \frac{\pi}{6} d_{\mathrm{m},i}^3$), equation (14) and (15) can be combined, giving the following equation:

$$B = \frac{4}{27}\ln^3\left(\frac{\rho_i}{\gamma_{\mathrm{sol},i} C_{\mathrm{sol},i}}\right) \tag{16}$$

It was found by He et al. that $\ln\left(A_i/J_{\mathrm{n},i}\right)$ was almost constant for various compounds (~5.15), allowing an approximation of the critical supersaturation as a function of crystal and solution properties. For leucine in an aqueous solution, the crystalline leucine density, $\rho_{\mathrm{leu}} = 1293$ mg/mL, and the aqueous solubility, $C_{\mathrm{sol,leu}} = 22$ mg/mL at 25 °C, can be used to calculate the critical supersaturation (Ordoubadi et al. 2020). In addition, the activity coefficient of water in the presence of leucine molecules at saturation was estimated to be 1 (Ordoubadi et al. 2020). With these values inserted into equation (13), the critical supersaturation of leucine in an aqueous solution was determined to be equal to 3.5, indicating that leucine is expected to nucleate instantaneously at a supersaturation of 3.5 in a water droplet.

Assuming that the same methodology can be extended to multi-solvent systems, the surface energy of a solute, i, in a co-solvent system, σ_i, can be approximated from

$$\sigma_i = \sum x_j \sigma_{i,j} \tag{17}$$

where x_j is the mole fraction of the jth solvent, and $\sigma_{i,j}$ is the surface tension in pure solvent j obtained from equation (15). Hence the thermodynamic parameter can be written as

$$B = \frac{4}{27}\ln^3\left[\prod_j\left(\frac{\rho_i}{\gamma_{\mathrm{sol},ij}C_{\mathrm{sol},ij}}\right)^{x_j}\right] \quad (18)$$

where $\gamma_{\mathrm{sol},ij}$ is the solvent activity coefficient at the solubility concentration of the solute in the jth solvent and $C_{\mathrm{sol},ij}$ is the solubility of the solute in the jth solvent. If these crystal and solution parameters are known, the critical supersaturation of the solute in a multi-solvent system can be determined. For example, given the leucine solubility of about 0.72 mg/mL in ethanol (PubChem n.d.) and assuming the activity coefficient to be equal to 1, the thermodynamic parameter of leucine in a water/ethanol mixture at 0.25/0.75 w/w water/ethanol is calculated to be about 30.7, and the solution of equation (13) gives the critical supersaturation $S_{\mathrm{n}} = 7.9$ or a concentration of 16.5 mg/mL with a solubility of about 2.1 mg/mL (Ordoubadi et al. 2019) in this solvent composition. Therefore, leucine is expected to nucleate instantaneously at the supersaturation of 7.9 in the water/ethanol 0.25/0.75 w/w solvent composition. We assume that nucleation commences instantaneously when the critical supersaturation point is reached and that the nucleation rate is sufficiently large. It is worth noting that this critical supersaturation point is not the onset of instability (the spinodal point), as this point falls inside the metastable region. Modeling or measurement of the unstable region is beyond the scope of this study. These supersaturation values were determined assuming the solvent composition remains constant; however, the solvent composition may change during spray drying, a subject that will be discussed later.

Particle Size Measurement

Particle size was measured in-process with an aerodynamic particle sizer (APS) (Model: 332100, TSI, Shoreview, USA) during spray drying (Wang et al. 2019). Briefly, a sampling port regulated by a two-way valve was opened immediately before every size measurement, and the APS was set to operate in-line at a standard flow rate of 5 L/min. The drying gas flow rate was reduced from the standard 0.5 m^3/min to 0.1 m^3/min during particle size measurement to prevent over-pressurizing the APS. Particle size was measured

every 15 min during spray drying, with each spray drying run typically taking 3-4 hours. Each measurement took 20 s to collect enough particles (>200 counts) to generate a particle size distribution.

Electron Microscopy

Microscopic images of the orifice plates were taken using a scanning electron microscope (SEM) (EVO M10, Zeiss, Jena, Germany). The orifice plates were placed on the SEM stubs for imaging. An accelerating voltage of 10 kV and working distance of 9-10 mm were used to capture the images. The orifice diameter was measured based on the SEM images using ImageJ software (ImageJ 1.53a, National Institutes of Health, USA).

Morphology of the spray-dried particles was analyzed using a field emission scanning electron microscope (FESEM) (Zeiss Sigma FESEM, Zeiss, Jena, Germany). Briefly, each particle sample was first placed on a SEM stub with a double-sided adhesive carbon tape to prevent an electron charging effect. The samples were then coated using a gold sputter (Desk II Gold Sputter, Denton Vacuum, NJ, USA) for 120 s. The in-lens detector, an accelerating voltage of 4-5 kV, and a working distance of 5-7 mm were used to capture the images.

Particle Crystallinity

A custom Raman spectroscopy system (Wang et al. 2017, 2019) was used to verify the solid phase of the spray-dried leucine particles. An aluminum sample holder with a conical cavity volume of 0.2 μL was used to load the collected sample powders for analysis. This setup utilized a 671 nm diode-pumped laser (Ventus 671, Laser Quantum, UK) with a maximum power of 500 mW. All sample powders were analyzed under a nitrogen atmosphere with less than 3% RH at room temperature (21 ± 1 °C). Raw L-leucine material was measured directly and used as the crystalline reference. The spectrum of the saturated aqueous solution of L-leucine after subtracting the spectrum of water was used as the Raman reference for amorphous L-leucine

(Feng et al. 2011) because an amorphous leucine powder reference could not be manufactured. Characteristic peaks of the reference spectra were used to determine the solid phase of L-leucine.

Results and Discussion

Multi-Orifice Plate

SEM images of the dual-orifice plate manufactured by Ga-FIB and two commercial orifice plates manufactured by laser drilling (Precision Pinhole, Edmund Optics, USA) are shown in Figure 2. The laser-drilled orifices had many irregular edges, and the geometry of one laser-drilled orifice was also irregular. These orifices with irregular edges and geometry were observed to produce deflected jets, leading to collisions between adjacent jets and subsequent loss of monodispersity in the spray-dried particles. By contrast, the dual-orifice plate manufactured by Ga-FIB had much cleaner orifice edges and regular orifice geometry. The diameter of the two orifices on the dual-orifice plate was measured as 31.2 ± 0.5 μm and 31.0 ± 0.6 μm respectively, showing that the two orifices were of a very similar size. These results can be expected since Ga-FIB provides higher resolution fabrication than laser-drilling. With clean orifice edges, regular geometry and similar orifice sizes, the dual-orifice plate is expected to produce monodisperse droplets and particles.

Figure 2

A typical aerodynamic diameter distribution of spray-dried leucine particles using the dual-orifice plate is shown in Figure 3. This figure illustrates that the particles spray dried using the dual-orifice plate had a narrow size distribution with a small geometric standard deviation (GSD) of 1.12. It has been reported that spray-dried particles with GSDs ranging from 1.1-1.3 are highly uniform in particle size (Ivey et al. 2018). The correspondence in GSD for the dual-orifice plate proves that it is capable of producing highly monodisperse droplets and spray-dried particles. It can be observed that the particle distribution is slightly asymmetric, which is a known phenomenon likely due to droplet collisions and coalescence (Wang et al. 2019; Ivey et al. 2018). The aerodynamic diameter of the spray-dried particles from doublets was calculated

to be around 4.2 μm, which explains the second small peak in the size distribution plot. It is possible to produce some very fine particles, probably dried from the satellite droplets generated by the monodisperse atomizer. This phenomenon has also been reported before (Ivey et al. 2018). However, in this study any such fine particles were negligible, since the satellite formation was minimized by careful selection of the excitation frequency, and thus they did not appear in the particle size distribution. An SEM image confirming the high uniformity in particle size of one batch of spray-dried leucine particles is shown in Figure 4. When the pressure difference across the orifice is the same, the dual-orifice plate should produce around twice as much liquid throughput as the single-orifice plate due to the same orifice diameter (30 μm) and a similar discharge coefficient (0.7-0.8). In the liquid throughput test where the pressure difference across the orifice was set to a normal operating value (170 ± 10 kPa) for both orifice plates, the dual-orifice plate produced a water throughput of 1.17 g/min, and the single-orifice plate produced a water throughput of 0.58 g/min. These results confirm that the dual-orifice plate had a roughly doubled throughput and, consequently, a doubled powder production rate compared with the single-orifice plate. The powder production rates and collection yields of three further spray drying runs using the dual-orifice plate are shown in Table 3. The actual powder production rates of the three spray drying runs had an average value of 23.8 ± 2.0 mg/hr, which was sufficient to produce the required sample mass for SEM and Raman spectroscopy analysis as well as the particle fragility testing within a reasonable spray drying time period. The collection yields of the three spray drying runs were in the range of 75-85%, indicating that there were losses of powders in the spray drying process probably due to wall deposition inside the spray dryer.

Figure 3

Figure 4

Table 3

Crystallinity of Spray-dried Particles

It has been reported that neat leucine particles spray dried from an aqueous solution are fully crystalline (Feng et al. 2011; Lucas et al. 1999). There has also been evidence showing that leucine particles spray dried from ethanol are likewise crystalline (Najafabadi et al. 2004). To confirm that different water/ethanol ratios and drying temperatures do not change the crystallinity of spray-dried leucine particles, four samples were selected for Raman spectroscopic analysis, including leucine spray dried from 0.25/0.75 w/w water/ethanol at 20 °C, 0.25/0.75 w/w water/ethanol at 80 °C, 0.5/0.5 w/w water/ethanol at 20 °C and 100% water at 80 °C. Raman spectra of the selected samples are shown in Figure 5 together with reference spectra for crystalline and amorphous leucine. Generally, crystalline and amorphous leucine show significantly different Raman spectra over the presented spectral region; the spectra of crystalline materials have sharper and more-defined peaks, while the corresponding peaks for the spectra of amorphous materials are broadened (Wang et al. 2014). As shown in Figure 5, the Raman spectra of all the measured samples are very similar to the reference spectrum for crystalline leucine. After subtraction of the reference for crystalline leucine, the characteristic peak of amorphous leucine around 750 cm^{-1} was not observed in the residual spectra. The residual spectrum for particles spray dried from 0.25/0.75 w/w water/ethanol at 20 °C is shown in Figure 5 as an example. Amorphous leucine content was not detected, or was below the detection limit of Raman spectroscopy (<1%), in the leucine particles spray dried from various water/ethanol ratios and drying temperatures in this study. Some minor differences can be observed in the spectra of spray-dried leucine compared with the reference spectrum of raw crystalline leucine material. The reference spectrum of raw crystalline leucine is considered as the polymorph I of leucine, which is expected under standard conditions (Feng et al. 2011). Since the transition temperature from polymorph I to polymorph II of leucine is 80 °C (Feng et al. 2011), the spray-dried leucine is very likely to still be in polymorph I. These minor differences might indicate some slight alteration of the unit cell geometry in spray-dried leucine particles compared with the raw crystalline leucine material, as reported before (Feng et al. 2011).

Figure 5

Crystal Size Analysis

SEM images of spray-dried leucine particles are shown in Figure 6. This figure illustrates the different crystal sizes on the surface of leucine particles that were spray dried from different solvent systems and at different drying temperatures. The well-defined domains in the size range of a few hundred nanometers or smaller are very likely individual crystals (Baldelli and Vehring 2016). These SEM images are presented roughly in order of decreasing crystal size in Figure 6(a-g). As shown in Figure 6(a), leucine particles spray dried from 0.25/0.75 w/w water/ethanol at 20 °C had the largest crystals compared with other cases. These thin flakes were often curved, a feature likely caused by deformation by the electron beam or by templating by the droplet surface. Single crystals with round contours have also been observed and discussed previously (Baldelli et al. 2016). The next case in Figure 6(b) is leucine spray dried from 0.25/0.75 w/w water/ethanol at 40 °C. The recognizable domains on the particle surface are smaller than in the previous case. The next three cases have similar crystal sizes. As shown in Figure 6(c-e), the domains are still noticeable but much smaller than in the first two cases. The last two cases in Figure 6(f-g) are also similar in that the surface of the particles is very smooth and can be explained by the presence of crystals that are too small to be noticeable. These differences in morphology of crystalline particles are supported by previous literature (Walton 2000), which states that crystalline particles can consist of sub-micron crystals or agglomerates with individual crystals bound together.

Figure 6

The solvent composition in the evaporating droplet versus drying time was determined using the numerical model and is shown in Figure 7. The water/ethanol ratio in the co-solvent system determines the evaporation rate of the droplet and the solubility of the solute. In most cases, the water/ethanol ratio will change with time during spray drying, although it can also remain constant in a special case, i.e. the iso-compositional point (Ordoubadi et al. 2019). The iso-compositional point is similar to the azeotrope during distillation, but the droplet temperature during spray drying is much lower than the boiling temperature of the azeotrope of water and ethanol (Ordoubadi et al. 2019). As shown in Figure 7(a), when the water/ethanol ratio is

initially 0.25/0.75, the mass fraction of ethanol generally remains constant throughout most of the spray drying process and decreases only close to the end, regardless of drying temperature. As a result, composition-dependent properties, including evaporation rate and solubility, will remain constant throughout most of the spray drying as well. This correspondence occurs because the water/ethanol ratio is close to the iso-compositional point, which is 0.23/0.77 w/w water/ethanol (Ordoubadi et al. 2019). When surface saturation of leucine reaches 1, which means nucleation can begin in the co-solvent system, the water/ethanol ratio is still approximately 0.25/0.75. When the surface saturation of leucine reaches the critical supersaturation of 7.9 in 0.25/0.75 w/w water/ethanol, initiating instantaneous nucleation, the water/ethanol ratio increases slightly to around 0.32/0.68 w/w. These instances are indicated by the red arrows in Figure 7(a). It is worth noting that the critical supersaturation of 7.9 is determined based on the 0.25/0.75 w/w water/ethanol solvent composition. The actual water/ethanol ratio at the supersaturation of 7.9 has a small deviation from the assumed water/ethanol ratio, which can influence the calculated supersaturation value. Therefore, iterations on the calculations of the critical supersaturation and the water/ethanol ratio at critical supersaturation can be used to find the accurate critical supersaturation value. However, since the initial deviation of the water/ethanol ratio is relatively small, and for simplicity of calculations, the critical supersaturation value was assumed to be 7.9 for the case of initial water/ethanol ratio of 0.25/0.75 w/w. In comparison, as shown in Figure 7(b), when the water/ethanol ratio is initially 0.5/0.5, the mass fraction of ethanol rapidly decreases to zero. The iso-compositional point requires a relatively high ethanol fraction of ~75% in the solvent to keep the solvent composition constant. When the initial ethanol fraction in the solvent is lower than 75%, the ethanol fraction in the solvent will keep decreasing until no ethanol remains and the solution in the droplet turns into an aqueous solution. In all three cases shown in Figure 7(b), leucine reaches surface saturation after the mass fraction of ethanol decreases to zero, which means the droplet has turned into a leucine aqueous solution before crystallization can commence. Afterwards, when leucine reaches the critical supersaturation of 3.5 in an aqueous solution, the solvent is still water only, confirming the critical supersaturation of 3.5 in this case. These instances are indicated by the red arrows in Figure 7(b). It is worth noting that the critical supersaturation varies

significantly depending on the solvent composition, which needs to be considered in determining the crystallization kinetics.

It is hypothesized that a longer time available for crystallization allows more time for crystal growth in general, thus leading to larger crystal size. In addition, crystal size is also related to the nucleation rate and growth rate. According to a previous study using the standard nucleation and growth models (Seydel et al. 2006), both the nucleation rate and growth rate can be affected by the supersaturation level of the solute; however, the growth rate is much less affected than the nucleation rate, and thus the change in growth rate can be ignored. If the time available for crystallization is relatively short, the supersaturation of the solute will increase rapidly to a high level. Since a higher supersaturation leads to a higher nucleation rate (Handscomb et al. 2009; Seydel et al. 2006), many small crystals are formed quickly while the already established crystals do not have time to grow. By contrast, if the time available for crystallization is relatively long, the supersaturation will increase slowly, giving the already established crystals more time to grow before more nucleation occurs. This theory is also consistent with the hypothesis that a longer time available for crystallization leads to larger crystal size. Two different times available for crystallization—one based on a surface saturation equal to 1 (t_c) and the other based on a surface saturation equal to the previously determined critical supersaturation values of 7.9 for water/ethanol 0.25/0.75 w/w and 3.5 for water/ethanol 0.5/0.5 and 1/0 w/w (t_c^*) —were both numerically modeled and are shown in Table 4, presented in the same order as in Figure 6. As can be seen in Table 4, t_c^* is shorter than t_c for each case, which can be expected since the critical supersaturation is reached later, while the relative magnitude of each case compared with other cases for t_c^* is actually consistent with t_c. A comparison of Figure 6 and Table 4 shows that leucine particles with larger crystals had relatively larger t_c and t_c^* than the ones with smaller crystals, while those with unnoticeable crystals had the smallest t_c and t_c^*. These results agree well with the theoretical predictions, confirming that both times available for crystallization can be used to qualitatively predict the crystal size of fully crystalline particles. Therefore, in the rest of this paper, either

t_c or t_c^* can be used as the time available for crystallization for qualitative analysis. However, the possibility of using the time available for crystallization to predict other crystallization processes such as polymorph changes was not explored in this study.

It is also important to understand how the process parameters, i.e. water/ethanol ratio and drying temperature, affect the time available for crystallization. Since the solubility of leucine in water/ethanol co-solvent is much lower than in an aqueous solution (Boraey et al. 2013), the saturation occurs much earlier in 0.25/0.75 w/w water/ethanol than in 0.5/0.5 w/w water/ethanol and pure water. Although the water/ethanol co-solvent increases the evaporation rate and shortens the time available for crystallization, the overall effect is that the time available for crystallization is longer in 0.25/0.75 w/w water/ethanol than in 0.5/0.5 w/w water/ethanol and pure water under the same drying temperature. Drying temperature mostly affects the evaporation rate of the droplet. Increasing the drying temperature increases the evaporation rate and simply shortens the time available for crystallization with the same co-solvent ratio.

Figure 7

Table 4

Particle Morphology and Formation

SEM images of three leucine particles spray dried in different conditions are shown in Figure 8 to illustrate three different particle morphologies. Figure 8(a) shows a highly porous leucine particle consisting of very large crystal flakes throughout the particle. Figure 8(b) shows a leucine particle consisting of medium-sized crystals. The particle was broken and the internal structure shows that the particle was still porous with crystals throughout the interior of the particle. Figure 8(c) shows a leucine particle with a hollow structure and a relatively smooth shell.

Figure 8

To understand and explain the morphology of the fully crystalline leucine particles, some particle formation theory should be reviewed. The dimensionless Peclet number, Pe, is very useful in explaining certain particle morphologies and is defined as (Boraey and Vehring 2014)

$$Pe_i = \frac{\kappa}{8D_i} \tag{19}$$

where κ is the evaporation rate and D_i is the diffusion coefficient of component i. This ratio describes how quickly the receding droplet surface shrinks compared to the diffusional motion of the solute inside the droplet. The surface enrichment, which is defined as the ratio of the solute concentration on the surface to the average solute concertation in the droplet for each component, can be approximated by (Vehring 2008; Vehring et al. 2007):

$$E_i = \frac{c_{s,i}}{c_{m,i}} = 1 + \frac{Pe_i}{5} + \frac{{Pe_i}^2}{100} - \frac{{Pe_i}^3}{4000} \tag{20}$$

This approximation assumes the steady state and is accurate within 1% when $Pe < 20$.

When the Peclet number is relatively small (close to 1 or less), the solute concentration is distributed almost evenly, with low surface enrichment. For solutes that do not crystalize, the droplet will likely be dried into a solid particle with a particle density close to the true density of the material. By contrast, when the Peclet number is much larger than 1, the solute concentration is much higher on the droplet surface while the solute concentration is very low inside the droplet, causing a much higher surface enrichment. In this case, a shell may be formed (Vehring 2008; Vehring et al. 2007). The Peclet numbers and surface enrichment calculated using numerical methods are shown in Figure 9. Here some of the Peclet numbers can be seen to change over time due to the changes in water/ethanol ratios, causing corresponding changes in the evaporation rate and diffusion coefficient. Consequently, in some of the cases the surface enrichments do not increase consistently over time, but rather increase first and then decrease, due to the decreases in the Peclet numbers. For all the cases the Peclet numbers are smaller than 3.5, and the surface enrichments are smaller than 1.8. However, it has been shown that leucine spray dried from an aqueous solution forms

hollow and low-density particles (Lucas et al. 1999), which cannot be explained by the calculated Peclet numbers and surface enrichment. One plausible explanation is that the Peclet number of the leucine increases drastically at the point of crystallization occurring at the surface at t_c or t_c^*, indicated by circles and squares on Figure 9, respectively. After the crystals are formed, the mobility of the leucine is no longer dependent on the diffusion of leucine molecules but rather on the diffusion of whole leucine crystals. The diffusion coefficient of leucine crystals is orders of magnitude smaller than that of leucine molecules, making the Peclet number much larger. The Peclet numbers of leucine crystals of different diameters (assuming spherical crystals) in pure water and ethanol at a drying temperature of 20 °C were calculated using numerical methods in conjunction with the Stokes-Einstein equation (Ziaee et al. 2019) and plotted in Figure 10. As shown in the figure, as the leucine nucleates and leucine crystals start to grow, the Peclet number of the leucine crystal increases rapidly to much larger than 1 in both water and ethanol solvent. For water/ethanol co-solvent the Peclet number will lie between these two extreme cases. Therefore, if the leucine crystals are formed at the droplet surface they cannot diffuse to the interior, and if the crystals are formed in the interior they will be swept up by the receding droplet surface, leading to the accumulation of leucine crystals at the droplet surface. When the volume fraction of the crystals at the droplet surface exceeds a certain level, a shell may be formed (Handscomb et al. 2009).

Figure 9

Figure 10

With the help of particle formation theory as well as the calculated times available for crystallization, the particle morphologies in Figure 8 can now be explained. If the time available for crystallization is relatively long and the supersaturation increases relatively slowly, there will be more than sufficient time for the crystals to grow to larger sizes and to the interior of the particle before more nucleation occurs. Of the three cases, the particle in Figure 8(a) had the longest time available for crystallization, which explains the porous structure with large crystals throughout the interior of the particle. If the time available for crystallization is relatively short and the supersaturation increases relatively quickly, the nanocrystals accumulated at the droplet surface do not have sufficient time to grow larger and to the interior of the particle before the particle

is dry. Of the three cases, the particle in Figure 8(c) had the shortest time available for crystallization, which explains its hollow structure with an empty interior and relatively smooth shell containing much smaller crystals. The particle in Figure 8(b) had a medium time available for crystallization and a medium increasing speed of supersaturation, which explains the medium-sized crystals, as the time available for crystallization in this case was still sufficient for the crystals to grow to the interior of the particle. These three cases are shown schematically in Figure 11.

Figure 11

Particle Fragility

Crystalline spray-dried particles with different interior structures are likely to have different physical properties, e.g. fragility. SEM images of two batches of leucine particles spray dried under different conditions are shown in Figure 12. Figure 12(a) shows that leucine particles consisting of large crystals throughout the interior structure were mostly unbroken, while Figure 12(b) shows many broken leucine particles (some of these indicated by red circles) which had a hollow structure with an empty interior and a thin shell consisting of nanocrystals. Leucine particles with a similar hollow structure were also found to be mostly fractured in a previous work (Lucas et al. 1999). These particles were likely broken during collection in the cyclone due to particle-particle or particle-wall collisions (Zhou et al. 2019), since leucine particles with a similar hollow structure collected by a membrane filter have been shown elsewhere to be unbroken (Ordoubadi et al. 2019). One possible explanation is that leucine particles consisting of large crystals bound together in the interior had a strong and stable structure, while leucine particles consisting of nanocrystals in the hollow shell lacked the interior structure, thus increasing their fragility. Keeping the particles unbroken is important in respiratory drug delivery applications because broken particles have reduced particle size and an exposed interior structure that may affect the product performance.

Figure 12

Conclusions

Compared with laser drilling, Ga-FIB milling is capable of manufacturing multi-orifice plates with cleaner orifice edges, regular orifice geometry and smaller orifice sizes while maintaining the monodispersity of spray-dried microparticles. Ga-FIB milling is also compatible with substances like stainless steel that are acceptable for pharmaceutical manufacturing. The powder production rate using the dual-orifice plate manufactured by Ga-FIB milling was sufficient for microscopic and spectroscopic analysis, and also for particle fragility testing. However, plates with more orifices are required for tests requiring larger sample masses, and smaller orifices are required for efficient manufacture of respirable products. Another limitation is that Ga-FIB milling is costly and time-consuming; therefore, more economical and efficient manufacturing techniques for the development of multi-orifice plates should also be considered.

Co-solvent ratio and drying temperature are two important parameters that control the crystallization kinetics in co-solvent spray drying. A higher water/ethanol ratio and higher drying temperature lead to a shorter time available for crystallization and, consequently, a more rapid increase in supersaturation. Increasing the time available for crystallization allows hollow and highly fragile particles consisting of nanocrystals to develop into stronger and more stable porous particles consisting of large crystals throughout the interior. Therefore, the co-solvent ratio and drying temperature must be well controlled in particle design and manufacturing processes to obtain target particle morphology and properties. The numerical methods used in this study are capable of determining the solvent environment as a function of time, which is also beneficial in studying the effects of the solvent environment on other crystallization characteristics including degree of polymorphism, nucleation rate, etc. It is also important to realize for the development of respirable dry powder products that even if particles have the same size, composition, and solid phase, they can still behave differently depending on the crystal size and interior structure. These findings and methods can be applied to other materials that form fully crystalline particles in spray drying in order to predict particle morphology and properties.

Acknowledgments

The authors would like to thank Shihong Xu and Peng Li of the Nanofabrication and Characterization Facility at the University of Alberta for their training in Ga-FIB milling.

References

Arpagaus, C., Collenberg, A., Rütti, D., Assadpour, E., and Jafari, S.M. (2018). Nano spray drying for encapsulation of pharmaceuticals. *Int. J. Pharm.,* 546(1–2):194–214.

Azhdarzadeh, M., Shemirani, F.M., Ruzycki, C.A., Baldelli, A., Ivey, J., Barona, D., Church, T., Lewis, D., Olfert, J.S., Finlay, W.H., and Vehring, R. (2016). An atomizer to generate monodisperse droplets from high vapor pressure liquids. *At. Sprays,* 26(2):121–134.

Baldelli, A., Power, R.M., Miles, R.E.H., Reid, J.P., and Vehring, R. (2016). Effect of crystallization kinetics on the properties of spray dried microparticles. *Aerosol Sci. Technol.,* 50(7):693–704.

Baldelli, A. and Vehring, R. (2016). Control of the radial distribution of chemical components in spray-dried crystalline microparticles. *Aerosol Sci. Technol.,* 50(10):1130–1142.

Bayvel, L. and Orzechowski, Z. (1993). Liquid Atomization. Taylor & Francis.

Boraey, M.A., Hoe, S., Sharif, H., Miller, D.P., Lechuga-Ballesteros, D., and Vehring, R. (2013). Improvement of the dispersibility of spray-dried budesonide powders using leucine in an ethanol-water cosolvent system. *Powder Technol.,* 236:171–178.

Boraey, M.A. and Vehring, R. (2014). Diffusion controlled formation of microparticles. *J. Aerosol Sci.,* 67:131–143.

Brenn, G., Durst, F., and Tropea, C. (1996). Monodisperse sprays for various purposes - Their production and characteristics. *Part. Part. Syst. Charact.,* 13(3):179–185.

Brenn, G., Helpiö, T., and Durst, F. (1997). A new apparatus for the production of monodisperse sprays at

high flow rates. *Chem. Eng. Sci.,* 52(2):237–244.

Carr, A.G., Mammucari, R., and Foster, N.R. (2011). Particle formation of budesonide from alcohol-modified subcritical water solutions. *Int. J. Pharm.,* 405(1–2):169–180.

Christoffersen, J., Rostrup, E., and Christoffersen, M.R. (1991). Relation between interfacial surface tension of electrolyte crystals in aqueous suspension and their solubility; a simple derivation based on surface nucleation. *J. Cryst. Growth,* 113(3–4):599–605.

Dumouchel, C. (2008). On the experimental investigation on primary atomization of liquid streams. *Exp. Fluids,* 45(3):371–422.

Feng, A.L., Boraey, M.A., Gwin, M.A., Finlay, P.R., Kuehl, P.J., and Vehring, R. (2011). Mechanistic models facilitate efficient development of leucine containing microparticles for pulmonary drug delivery. *Int. J. Pharm.,* 409(1–2):156–163.

Fu, N., Zhou, Z., Jones, T.B., Tan, T.T.Y., Wu, W.D., Lin, S.X., Chen, X.D., and Chan, P.P.Y. (2011). Production of monodisperse epigallocatechin gallate (EGCG) microparticles by spray drying for high antioxidant activity retention. *Int. J. Pharm.,* 413(1–2):155–166.

Gharsallaoui, A., Roudaut, G., Chambin, O., Voilley, A., and Saurel, R. (2007). Applications of spray-drying in microencapsulation of food ingredients: An overview. *Food Res. Int.,* 40(9):1107–1121.

Handscomb, C.S., Kraft, M., and Bayly, A.E. (2009). A new model for the drying of droplets containing suspended solids. *Chem. Eng. Sci.,* 64(4):628–637.

He, G., Bhamidi, V., Tan, R.B.H., Kenis, P.J.A., and Zukoski, C.F. (2006). Determination of critical supersaturation from microdroplet evaporation experiments. *Cryst. Growth Des.,* 6(5):1175–1180.

Ivey, J.W. (2018). Particle Formation from Evaporating Microdroplets for Inhaled Drug Delivery. University of Alberta.

Ivey, J.W., Bhambri, P., Church, T.K., Lewis, D.A., and Vehring, R. (2018). Experimental investigations of particle formation from propellant and solvent droplets using a monodisperse spray dryer. *Aerosol Sci. Technol.,* 52(6):702–716.

Lee, Y.Y., Wu, J.X., Yang, M., Young, P.M., Van Den Berg, F., and Rantanen, J. (2011). Particle size

dependence of polymorphism in spray-dried mannitol. *Eur. J. Pharm. Sci.,* 44(1–2):41–48.

Li, L., Sun, S., Parumasivam, T., Denman, J.A., Gengenbach, T., Tang, P., Mao, S., and Chan, H.K. (2016). L-Leucine as an excipient against moisture on in vitro aerosolization performances of highly hygroscopic spray-dried powders. *Eur. J. Pharm. Biopharm.,* 102:132–141.

Liu, W., Chen, X.D., and Selomulya, C. (2015). On the spray drying of uniform functional microparticles. *Particuology,* 22:1–12.

Liu, W., Wu, W.D., Selomulya, C., and Chen, X.D. (2011). Uniform chitosan microparticles prepared by a novel spray-drying technique. *Int. J. Chem. Eng.,* 2011.

Lu, W., Wang, S., Lin, R., Yang, X., and Cheng, Z. (2020). Unveiling the importance of process parameters on droplet shrinkage and crystallization behaviors of easily crystalline material during spray drying. *Dry. Technol.,* 0(0):1–11.

Lucas, P., Kerry, A., Potter, U.J., and Staniforth, J.N. (1999). Enhancement of Small Particle Size Dry Powder Aerosol Formulations using an Ultra Low Density Additive. *Pharm. Res.,* 16:1643–1647.

McDonagh, A.F. and Tajber, L. (2019). The control of paracetamol particle size and surface morphology through crystallisation in a spray dryer. *Adv. Powder Technol.,* 31(1):287–299.

Mehanna, M.M., Mohyeldin, S.M., and Elgindy, N.A. (2014). Respirable nanocarriers as a promising strategy for antitubercular drug delivery. *J. Control. Release,* 187:183–197.

Najafabadi, A.R., Gilani, K., Barghi, M., and Rafiee-Tehrani, M. (2004). The effect of vehicle on physical properties and aerosolisation behaviour of disodium cromoglycate microparticles spray dried alone or with L-leucine. *Int. J. Pharm.,* 285(1–2):97–108.

Ordoubadi, M., Gregson, F.K.A., Melhem, O., Barona, D., Miles, R.E.H., D'Sa, D., Gracin, S., Lechuga-Ballesteros, D., Reid, J.P., Finlay, W.H., and Vehring, R. (2019). Multi-Solvent Microdroplet Evaporation: Modeling and Measurement of Spray-Drying Kinetics with Inhalable Pharmaceutics. *Pharm. Res.,* 36(7).

Ordoubadi, M., Gregson, F.K.A., Wang, H., Nicholas, M., Gracin, S., Lechuga-Ballesteros, D., Reid, J.P., Finlay, W.H., and Vehring, R. (2020). On the particle formation of leucine in spray drying of

inhalable microparticles. *Int. J. Pharm.,* (November):120102.

Patel, K.C. and Chen, X.D. (2007). Production of spherical and uniform-sized particles using a laboratory ink-jet spray dryer. *Asia-Pacific J. Chem. Eng.,* 2(5):415–430.

PubChem (n.d.). Leucine. Available at https://pubchem.ncbi.nlm.nih.gov/compound/Leucine (Accessed 1 December 2020).

Rayleigh, Lord (1878). On the Instability of Jets. *Proc. London Math. Soc.,* s1-10(1):4–13.

Rogers, S., Fang, Y., Qi Lin, S.X., Selomulya, C., and Dong Chen, X. (2012a). A monodisperse spray dryer for milk powder: Modelling the formation of insoluble material. *Chem. Eng. Sci.,* 71:75–84.

Rogers, S., Wu, W.D., Lin, S.X.Q., and Chen, X.D. (2012b). Particle shrinkage and morphology of milk powder made with a monodisperse spray dryer. *Biochem. Eng. J.,* 62:92–100.

Schmitz-Schug, I., Kulozik, U., and Foerst, P. (2016). Modeling spray drying of dairy products - Impact of drying kinetics, reaction kinetics and spray drying conditions on lysine loss. *Chem. Eng. Sci.,* 141:315–329.

Seydel, P., Blömer, J., and Bertling, J. (2006). Modeling particle formation at spray drying using population balances. *Dry. Technol.,* 24(2):137–146.

Shishir, M.R.I. and Chen, W. (2017). Trends of spray drying: A critical review on drying of fruit and vegetable juices. *Trends Food Sci. Technol.,* 65:49–67.

Sosnik, A. and Seremeta, K.P. (2015). Advantages and challenges of the spray-drying technology for the production of pure drug particles and drug-loaded polymeric carriers. *Adv. Colloid Interface Sci.,* 223:40–54.

Tontul, I. and Topuz, A. (2017). Spray-drying of fruit and vegetable juices: Effect of drying conditions on the product yield and physical properties. *Trends Food Sci. Technol.,* 63:91–102.

Vehring, R. (2008). Pharmaceutical particle engineering via spray drying. *Pharm. Res.,* 25(5):999–1022.

Vehring, R., Foss, W.R., and Lechuga-Ballesteros, D. (2007). Particle formation in spray drying. *J. Aerosol Sci.,* 38(7):728–746.

Walton, D.E. (2000). The morphology of spray-dried particles a qualitative view. *Dry. Technol.,*

18(9):1943–1986.

Wang, H., Barona, D., Oladepo, S., Williams, L., Hoe, S., Lechuga-Ballesteros, D., and Vehring, R. (2017). Macro-Raman spectroscopy for bulk composition and homogeneity analysis of multi-component pharmaceutical powders. *J. Pharm. Biomed. Anal.,* 141:180–191.

Wang, H., Boraey, M.A., Williams, L., Lechuga-Ballesteros, D., and Vehring, R. (2014). Low-frequency shift dispersive Raman spectroscopy for the analysis of respirable dosage forms. *Int. J. Pharm.,* 469(1):197–205.

Wang, H., Nobes, D.S., and Vehring, R. (2019). Particle Surface Roughness Improves Colloidal Stability of Pressurized Pharmaceutical Suspensions. *Pharm. Res.,* 36(3):1–17.

Wu, W.D., Patel, K.C., Rogers, S., and Chen, X.D. (2007). Monodisperse droplet generators as potential atomizers for spray drying technology. *Dry. Technol.,* 25(12):1907–1916.

Zhou, H., Hu, Z., Zhang, Q., Wang, Q., and Lv, X. (2019). Numerical study on gas-solid flow characteristics of ultra-light particles in a cyclone separator. *Powder Technol.,* 344:784–796.

Ziaee, A., Albadarin, A.B., Padrela, L., Femmer, T., O'Reilly, E., and Walker, G. (2019). Spray drying of pharmaceuticals and biopharmaceuticals: Critical parameters and experimental process optimization approaches. *Eur. J. Pharm. Sci.,* 127(January 2019):300–318.

List of Figure captions

Figure 1. Schematic of the vibrating orifice atomizer using a dual-orifice plate.

Figure 2. SEM image of orifice plate: (a) dual-orifice plate manufactured by Ga-FIB (b) commercial single-orifice plates manufactured by laser drilling.

Figure 3. Aerodynamic diameter distribution of leucine particles spray dried from 0.25/0.75 w/w water/ethanol at 20 °C with a mass median aerodynamic diameter (MMAD) of 3.33 μm and geometric standard deviation (GSD) of 1.12.

Figure 4. SEM image of leucine particles spray dried from 0.25/0.75 w/w water/ethanol at 20°C using the dual-orifice plate.

Figure 5. Raman spectra of leucine particles spray dried from (a) 0.25/0.75 w/w water/ethanol at 20°C, (b) 0.25/0.75 w/w water/ethanol at 80 °C, (c) 0.5/0.5 w/w water/ethanol at 20 °C, (d) 100% water at 80

°C, and spectra for (e) reference crystalline leucine, (f) reference amorphous leucine, and (g) residual spectrum achieved by subtracting reference crystalline leucine from the spectrum of leucine particles spray dried from 0.25/0.75 w/w water/ethanol at 20 °C.

Figure 6. SEM images of leucine particles spray dried from (a) 0.25/0.75 w/w water/ethanol at 20 °C, (b) 0.25/0.75 w/w water/ethanol at 40 °C, (c) 0.25/0.75 w/w water/ethanol at 80 °C, (d) 0.5/0.5 w/w water/ethanol at 20 °C, (e) 0.5/0.5 w/w water/ethanol at 40 °C, (f) 0.5/0.5 w/w water/ethanol at 80°C and (g) 100% water at 80 °C. The scale bar applies to all the images.

Figure 7. Mass fraction of ethanol and surface saturation of leucine in the evaporating droplet with initial water/ethanol ratio of (a) 0.25/0.75 w/w and (b) 0.5/0.5 w/w at a drying temperature of (i) 20 °C, (ii) 40 °C, and (iii) 80 °C. Red arrows point to the mass fraction of ethanol when surface saturation reaches 1 and the critical supersaturation (7.9 in (a) and 3.5 in (b)).

Figure 8. SEM images of leucine particles spray dried from (a) 0.25/0.75 w/w water/ethanol at 20 °C, (b) 0.5/0.5 w/w water/ethanol at 20 °C, and (c) 0.5/0.5 w/w water/ethanol at 80 °C.

Figure 9. Peclet number (top) and surface enrichment (bottom) as a function of time for all the cases. L: Leucine; W: Water; E: Ethanol. Circles indicate the points at which surface saturation reaches 1, and squares indicate the point at which surface saturation reaches the critical supersaturation.

Figure 10. Peclet number of leucine at drying temperature of 20 °C as a function of crystal diameter in water and ethanol.

Figure 11. Schematic of the particle formation process for the three cases with different times available for crystallization.

Figure 12. SEM images of spray-dried leucine particles from (a) 0.25/0.75 w/w water/ethanol at 20 °C (b) 100% water at 80 °C. Red circles indicate some of the broken particles.

Table 1. Spray drying parameters

Parameter	Value
Pressure difference across orifice	100-200 kPa
Micro-orifice diameter	30 μm
Feed solution temperature	20 ± 1°C
Inlet/outlet temperature	20°C/20°C, 40°C/32°C, 80°C/56°C (±1°C)
Disperser cap orifice diameter	3.0 mm
Dispersing gas pressure	275 kPa
Dispersing gas flow rate	0.293 g/s
Dispersing gas temperature	20 ± 1°C
Drying gas flow rate	0.5 m^3/min
Piezoelectric driving frequency	90 ± 10 kHz
Drying chamber diameter	0.2 m
Drying chamber height	1.85 m

Table 2. Formulations with drying temperatures

Feed concentration of leucine (mg/mL)	Water/ethanol w/w	Drying temperature (°C)
0.5	0.25/0.75	20
	0.25/0.75	40
	0.25/0.75	80
	0.5/0.5	20
	0.5/0.5	40
	0.5/0.5	80
	1/0	80

Table 3. Powder production rate and collection yield of three spray drying runs using the dual-orifice plate

Formulations	Actual Powder Production Rate (mg/hr)	Theoretical Powder Production Rate (mg/hr)	Collection Yield
L-0.25W/0.75E-20 °C	21.8	25.9	84.2%
L-0.25W/0.75E-40 °C	26.5	31.2	84.9%
L-0.25W/0.75E-80 °C	23.2	29.7	78.1%

L: Leucine; W: Water; E: Ethanol.

Table 4. Predicted time available for crystallization for all the cases

water/ethanol w/w	0.25/0.75	0.25/0.75	0.25/0.75	0.5/0.5	0.5/0.5	0.5/0.5	1/0
Drying temperature (°C)	20	40	80	20	40	80	80
Droplet lifetime (s)	1.19	0.68	0.33	1.90	1.06	0.50	0.74
Time to reach saturation (s)	0.55	0.30	0.13	1.66	0.93	0.44	0.68
Time to reach critical supersaturation (s)	1.02	0.58	0.28	1.85	1.03	0.48	0.73
t_c (s)	0.64	0.38	0.20	0.24	0.13	0.06	0.06
t_c^* (s)	0.17	0.10	0.05	0.05	0.03	0.02	0.01

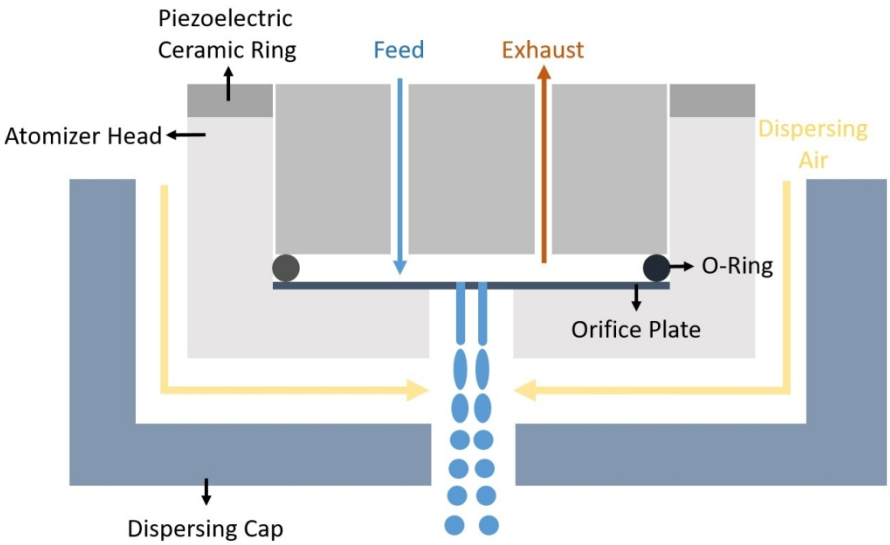

Figure 1. Schematic of the vibrating orifice atomizer using a dual-orifice plate.

383x210mm (96 x 96 DPI)

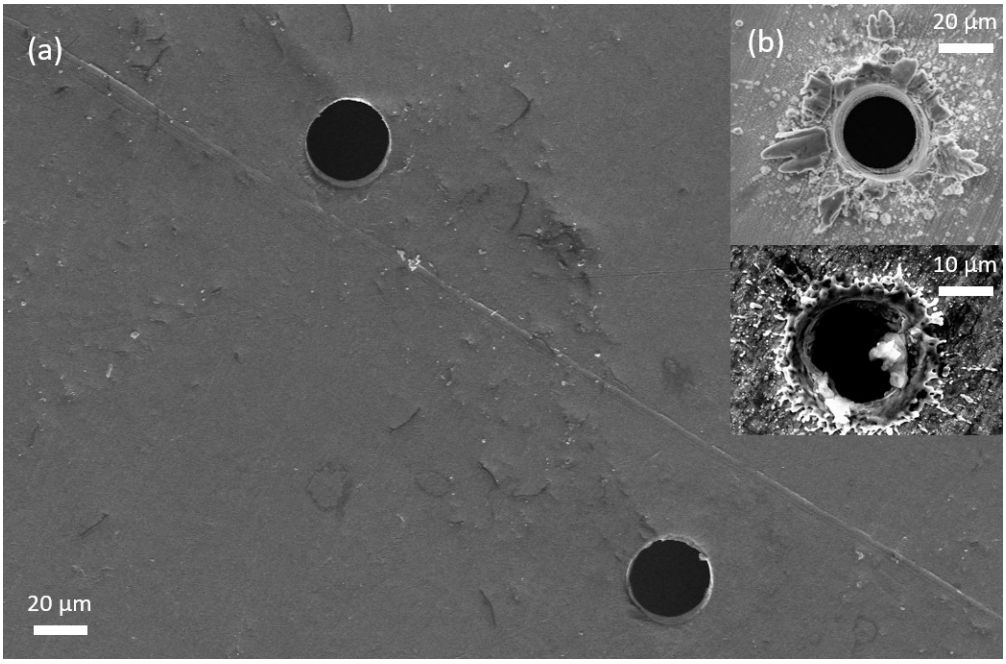

Figure 2. SEM image of orifice plate: (a) dual-orifice plate manufactured by Ga-FIB (b) commercial single-orifice plates manufactured by laser drilling.

275x180mm (96 x 96 DPI)

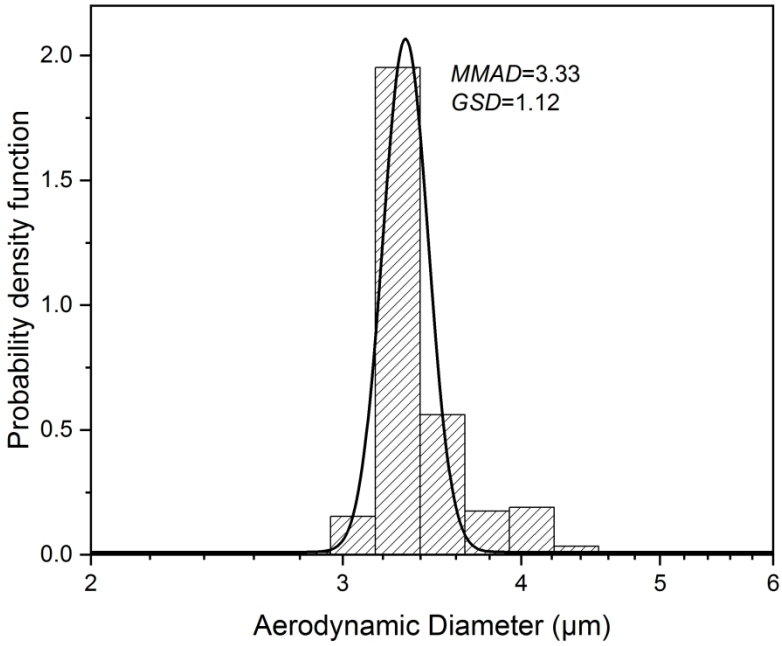

Figure 3. Aerodynamic diameter distribution of leucine particles spray dried from 0.25/0.75 w/w water/ethanol at 20 °C with a mass median aerodynamic diameter (MMAD) of 3.33 μm and geometric standard deviation (GSD) of 1.12.

272x208mm (300 x 300 DPI)

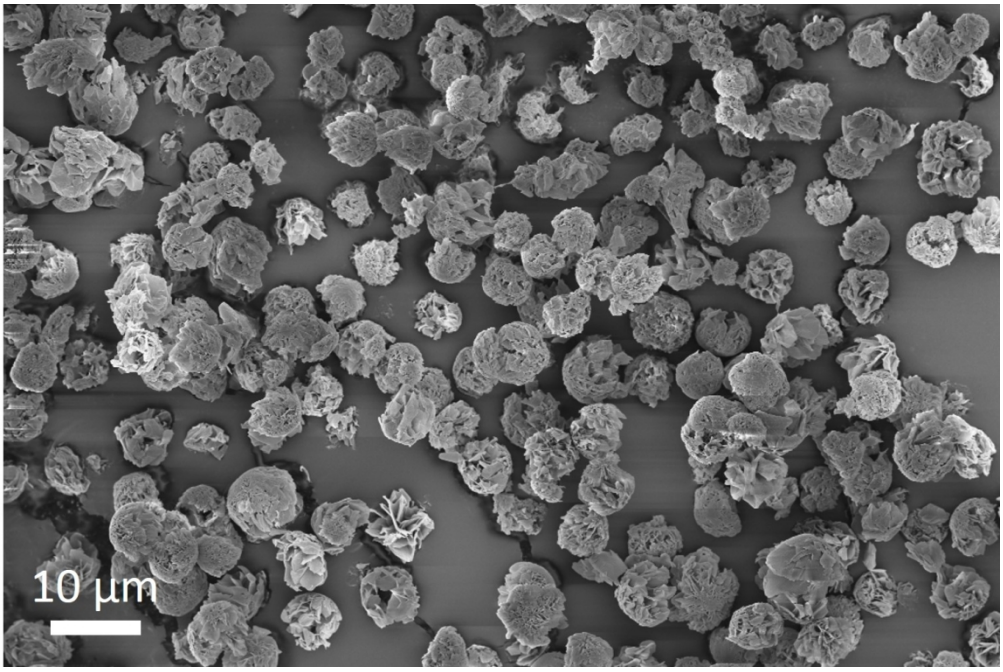

Figure 4. SEM image of leucine particles spray dried from 0.25/0.75 w/w water/ethanol at 20°C using the dual-orifice plate.

254x168mm (150 x 150 DPI)

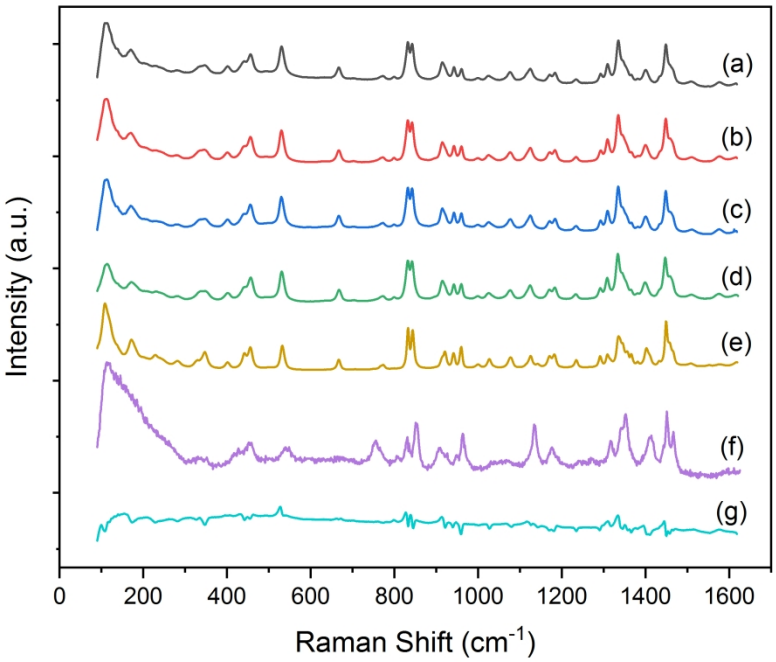

Figure 5. Raman spectra of leucine particles spray dried from (a) 0.25/0.75 w/w water/ethanol at 20°C, (b) 0.25/0.75 w/w water/ethanol at 80 °C, (c) 0.5/0.5 w/w water/ethanol at 20 °C, (d) 100% water at 80 °C, and spectra for (e) reference crystalline leucine, (f) reference amorphous leucine, and (g) residual spectrum achieved by subtracting reference crystalline leucine from the spectrum of leucine particles spray dried from 0.25/0.75 w/w water/ethanol at 20 °C.

271x203mm (300 x 300 DPI)

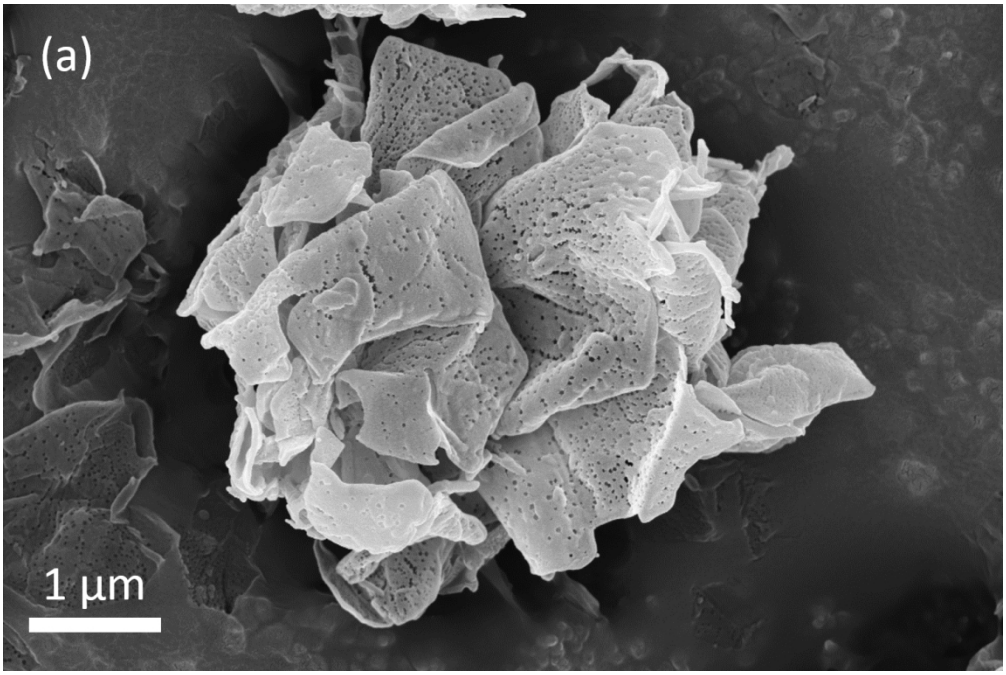

Figure 6. SEM images of leucine particles spray dried from (a) 0.25/0.75 w/w water/ethanol at 20 °C, (b) 0.25/0.75 w/w water/ethanol at 40 °C, (c) 0.25/0.75 w/w water/ethanol at 80 °C, (d) 0.5/0.5 w/w water/ethanol at 20 °C, (e) 0.5/0.5 w/w water/ethanol at 40 °C, (f) 0.5/0.5 w/w water/ethanol at 80°C and (g) 100% water at 80 °C. The scale bar applies to all the images.

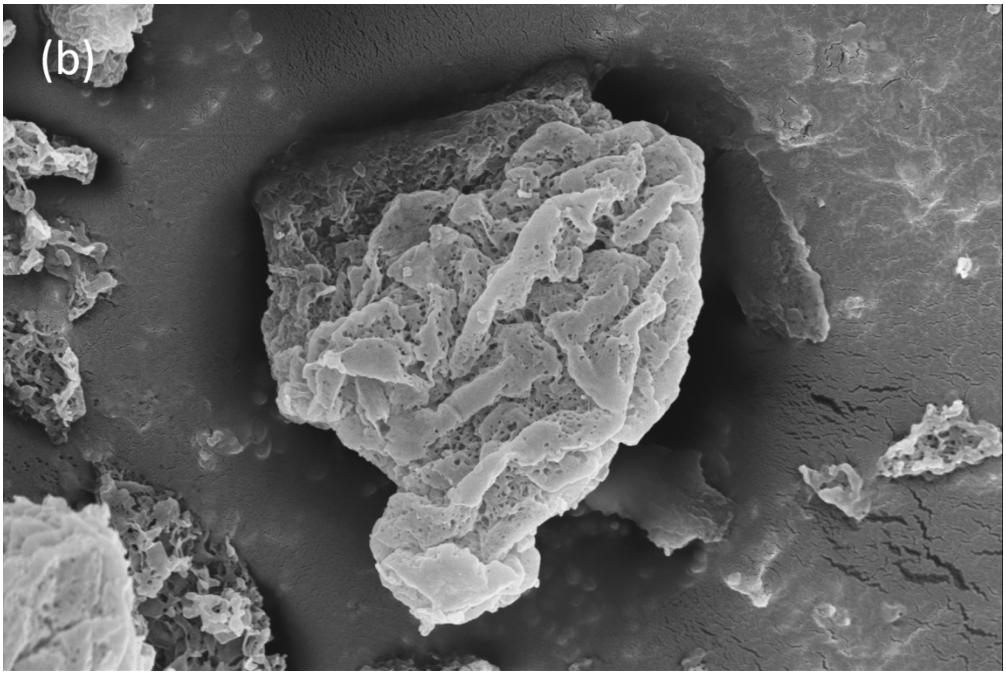
(b)

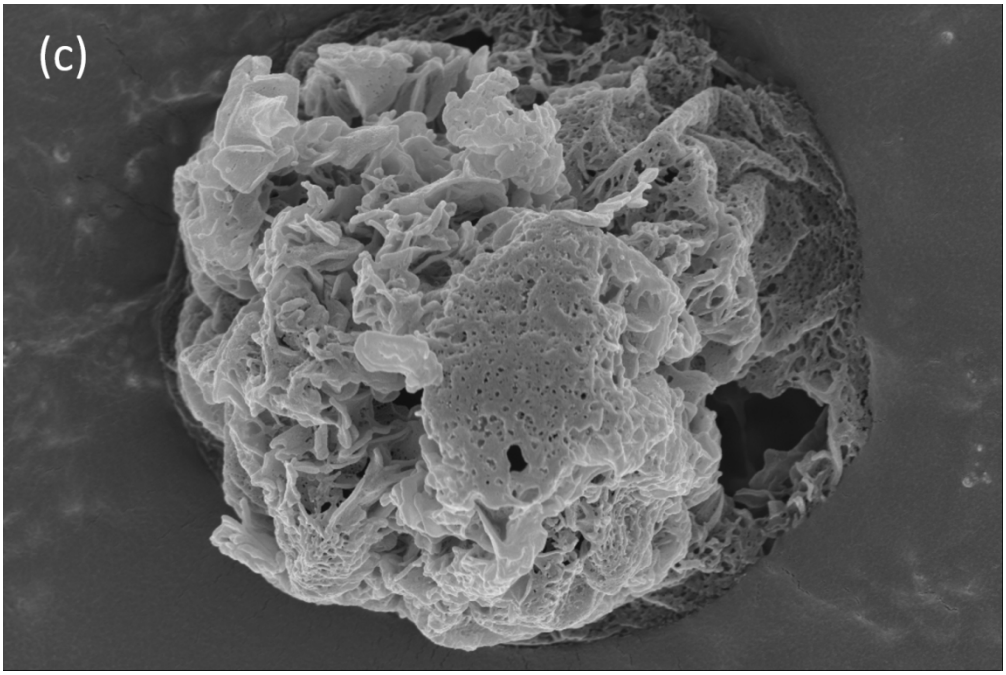
(c)

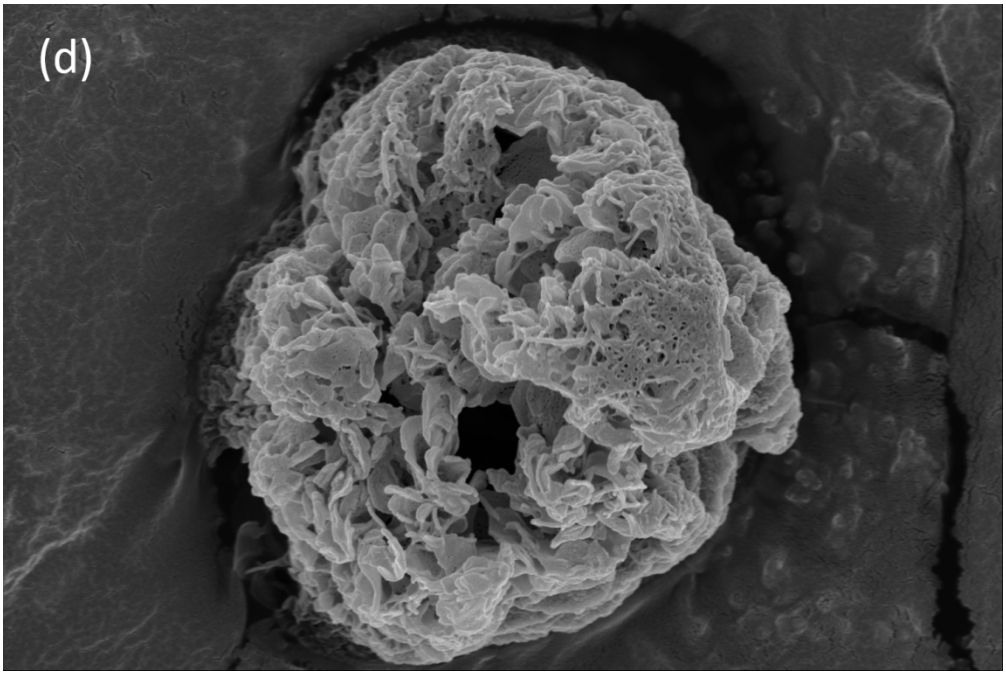
(d)

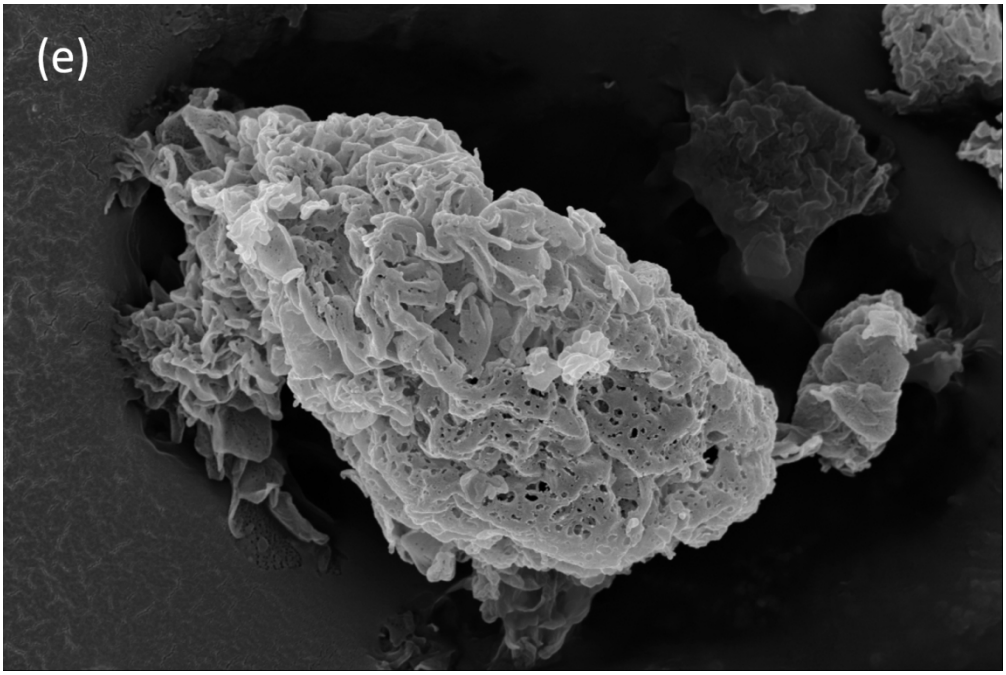
(e)

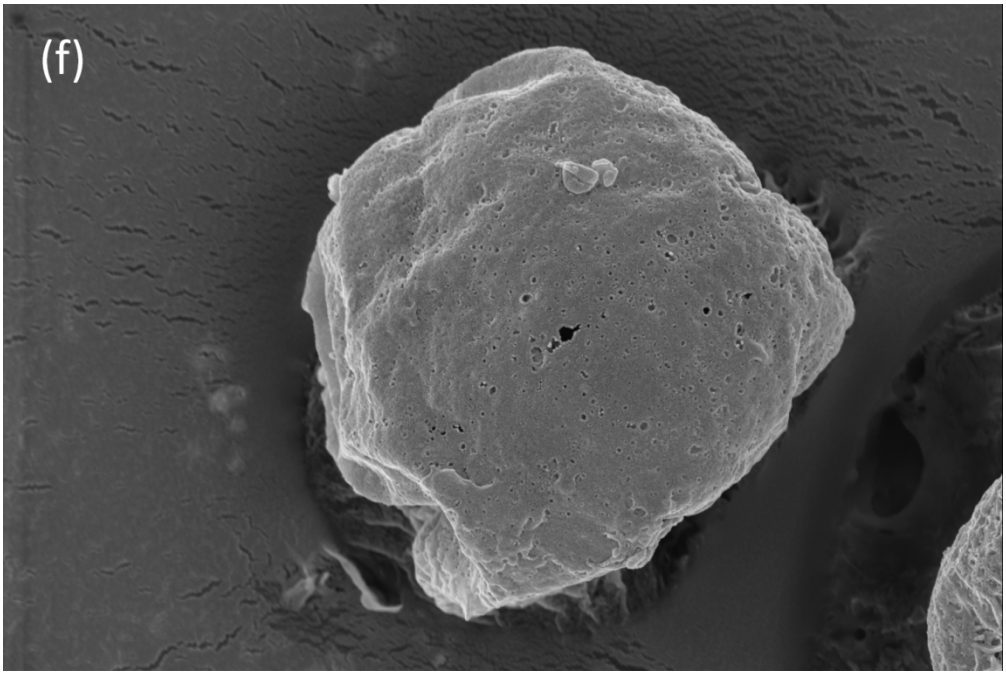
(f)

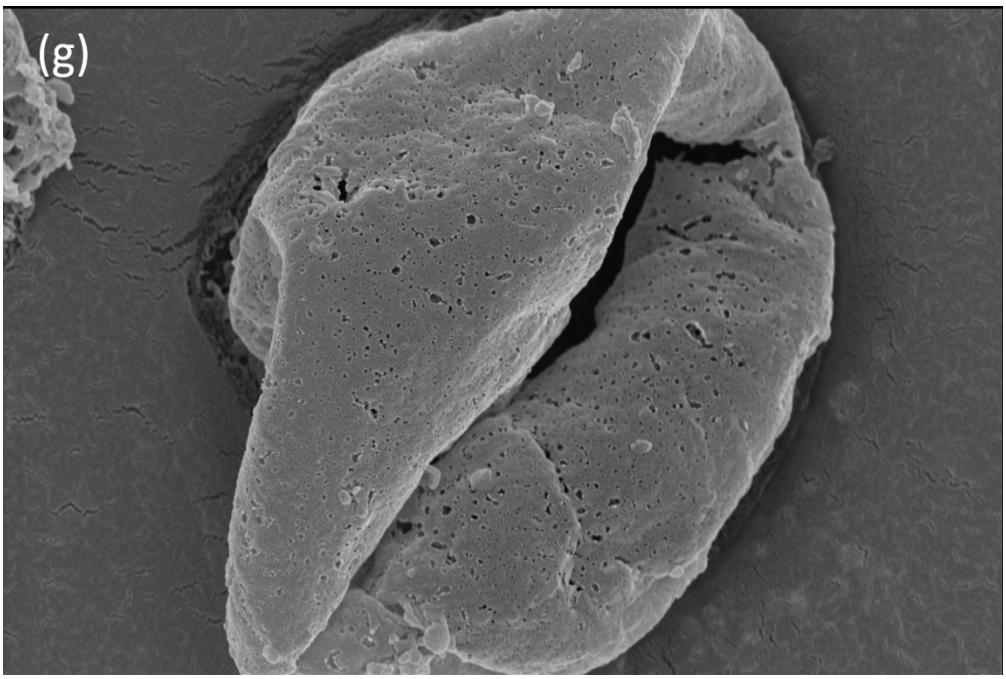
(g)

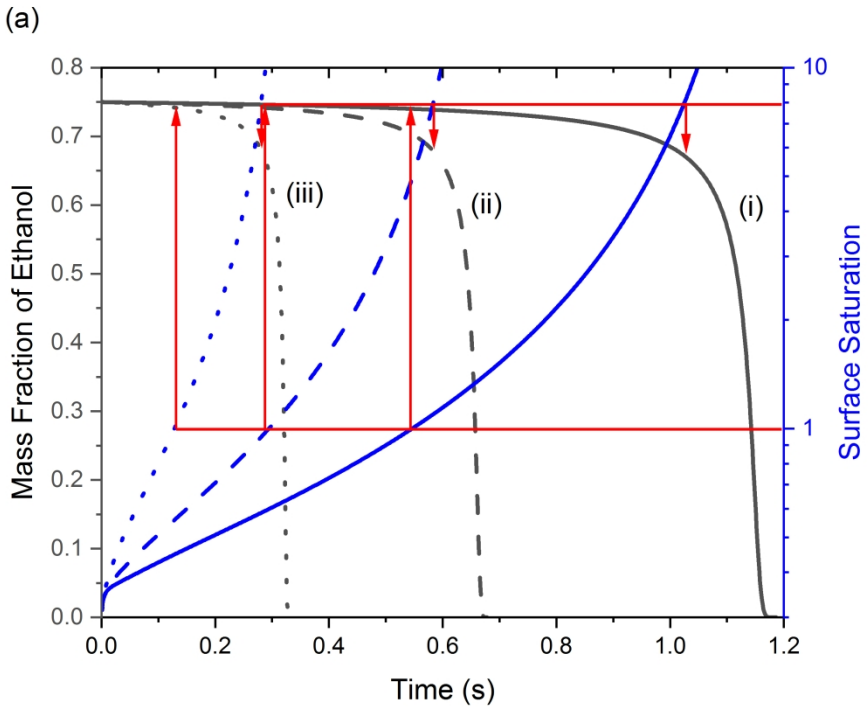

Figure 7. Mass fraction of ethanol and surface saturation of leucine in the evaporating droplet with initial water/ethanol ratio of (a) 0.25/0.75 w/w and (b) 0.5/0.5 w/w at a drying temperature of (i) 20 °C, (ii) 40 °C, and (iii) 80 °C. Red arrows point to the mass fraction of ethanol when surface saturation reaches 1 and the critical supersaturation (7.9 in (a) and 3.5 in (b)).

272x208mm (300 x 300 DPI)

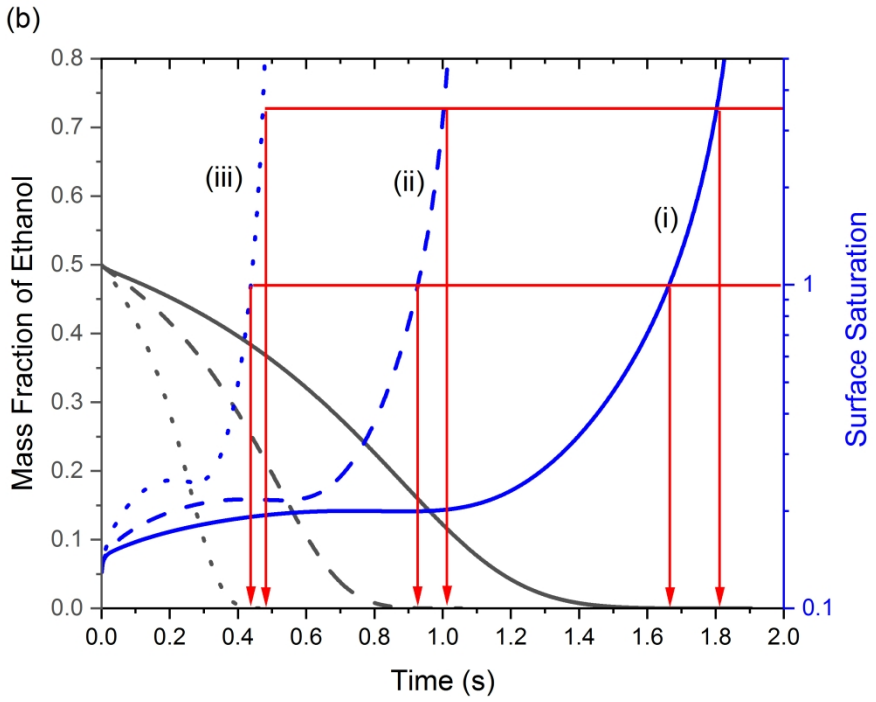

272x208mm (300 x 300 DPI)

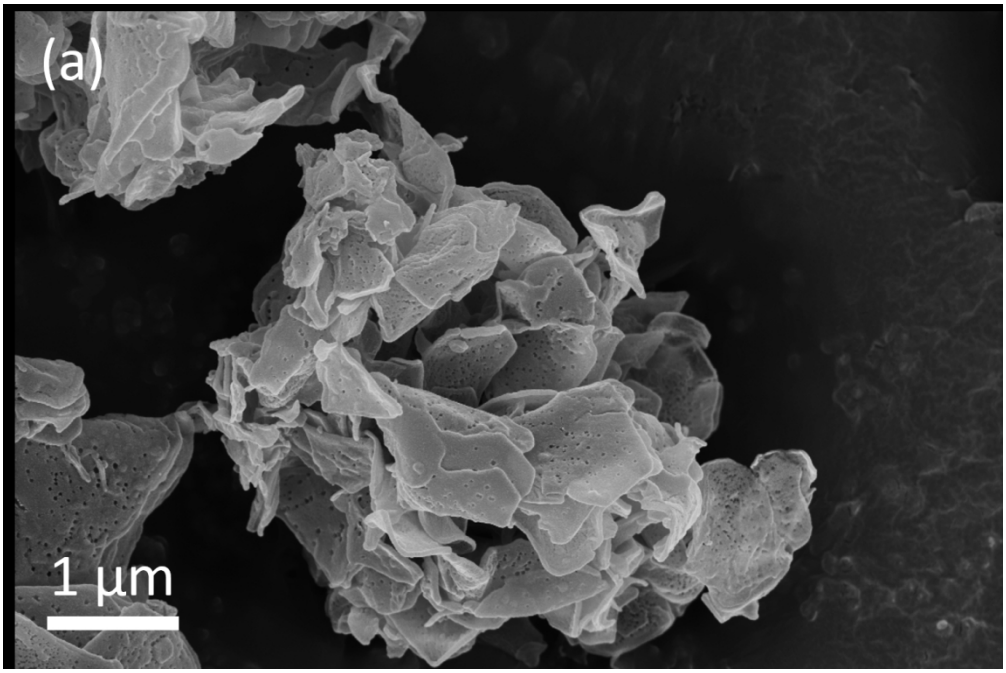

Figure 8. SEM images of leucine particles spray dried from (a) 0.25/0.75 w/w water/ethanol at 20 °C, (b) 0.5/0.5 w/w water/ethanol at 80 °C.

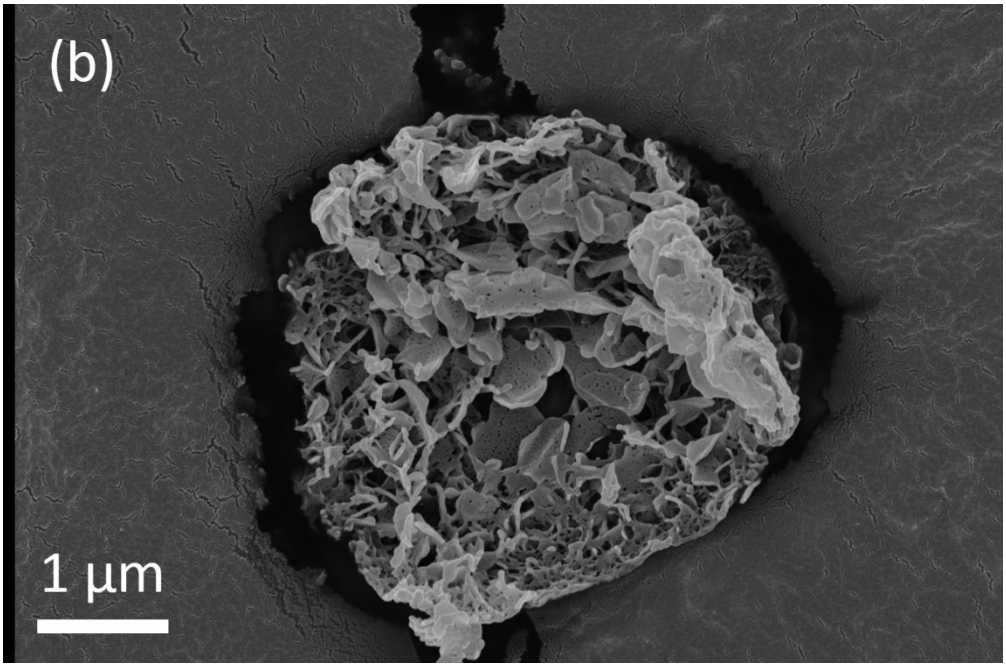
(b)
1 µm

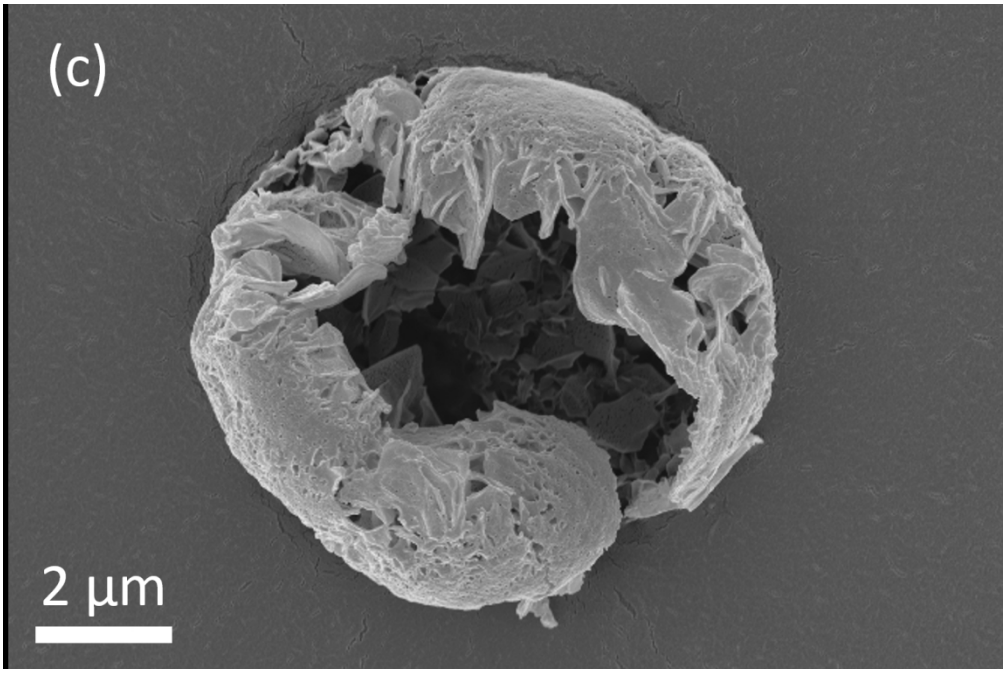
(c)
2 µm

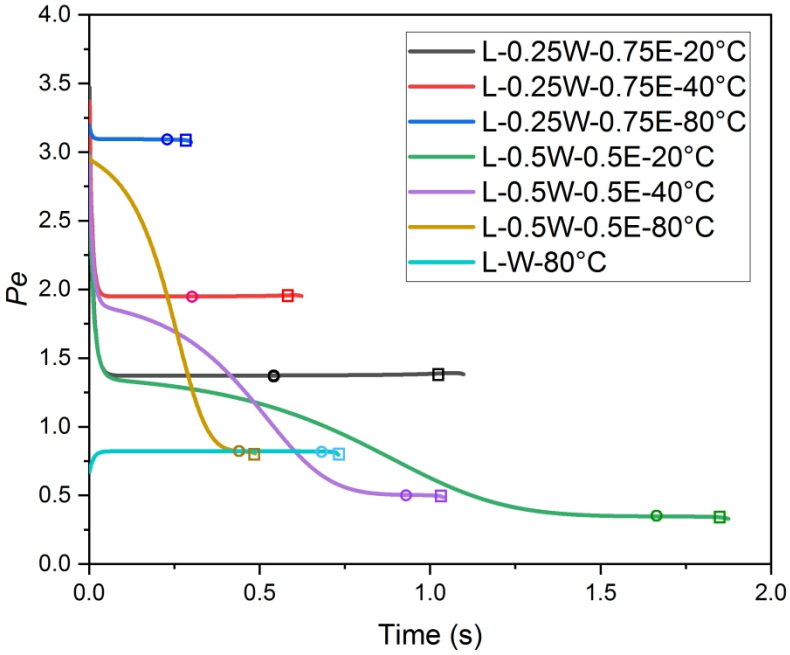

Figure 9. Peclet number (top) and surface enrichment (bottom) as a function of time for all the cases. L: Leucine; W: Water; E: Ethanol. Circles indicate the points at which surface saturation reaches 1, and squares indicate the point at which surface saturation reaches the critical supersaturation.

272x208mm (300 x 300 DPI)

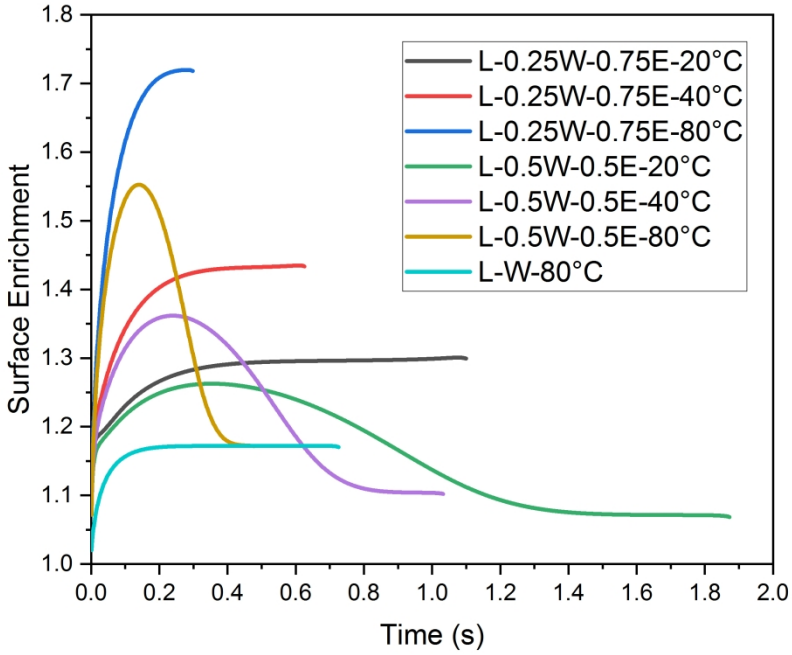

272x208mm (300 x 300 DPI)

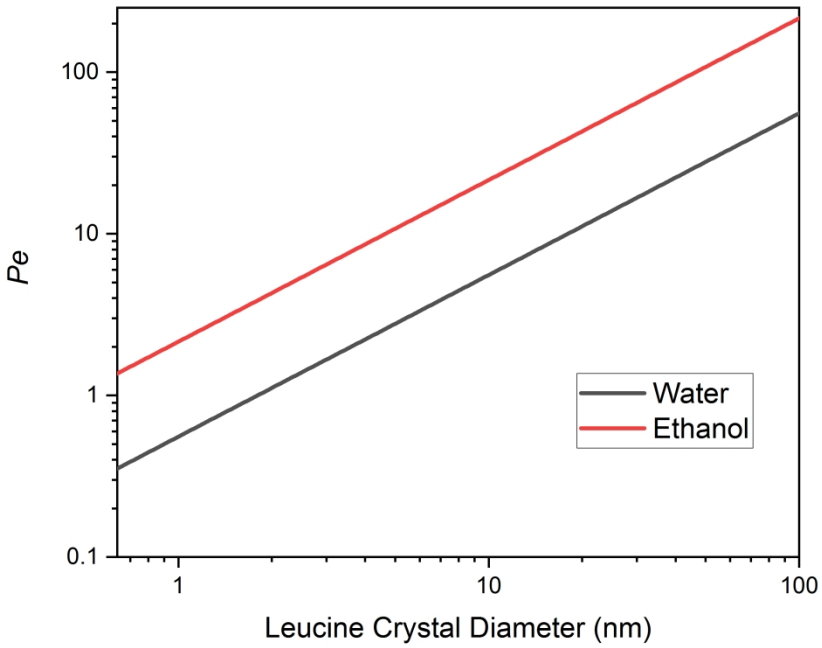

Figure 10. Peclet number of leucine at drying temperature of 20 °C as a function of crystal diameter in water and ethanol.

272x208mm (300 x 300 DPI)

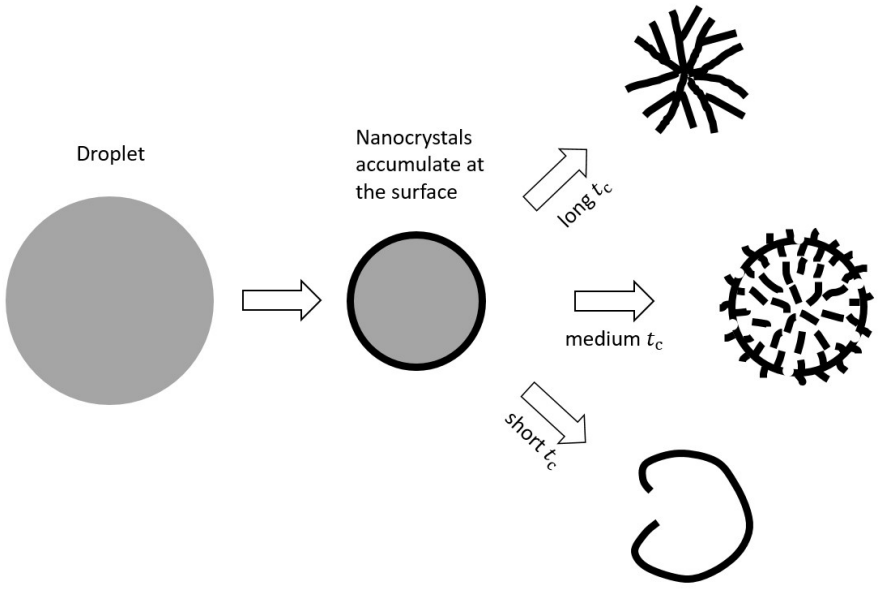

Figure 11. Schematic of the particle formation process for the three cases with different times available for crystallization.

325x203mm (96 x 96 DPI)

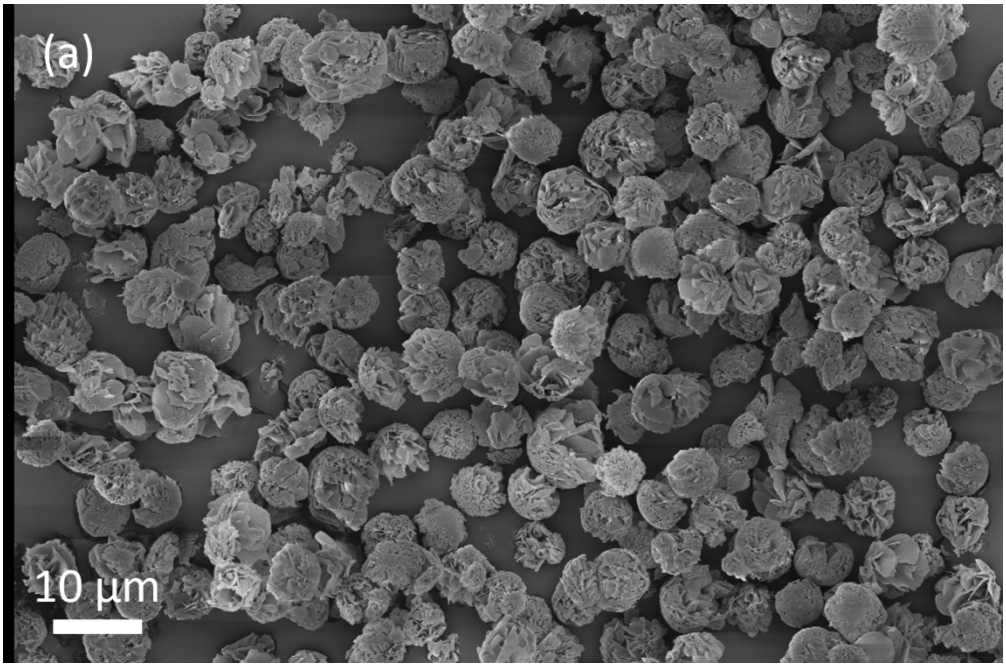

Figure 12. SEM images of spray-dried leucine particles from (a) 0.25/0.75 w/w water/ethanol at 20 °C (b) 100% water at 80 °C. Red circles indicate some of the broken particles.

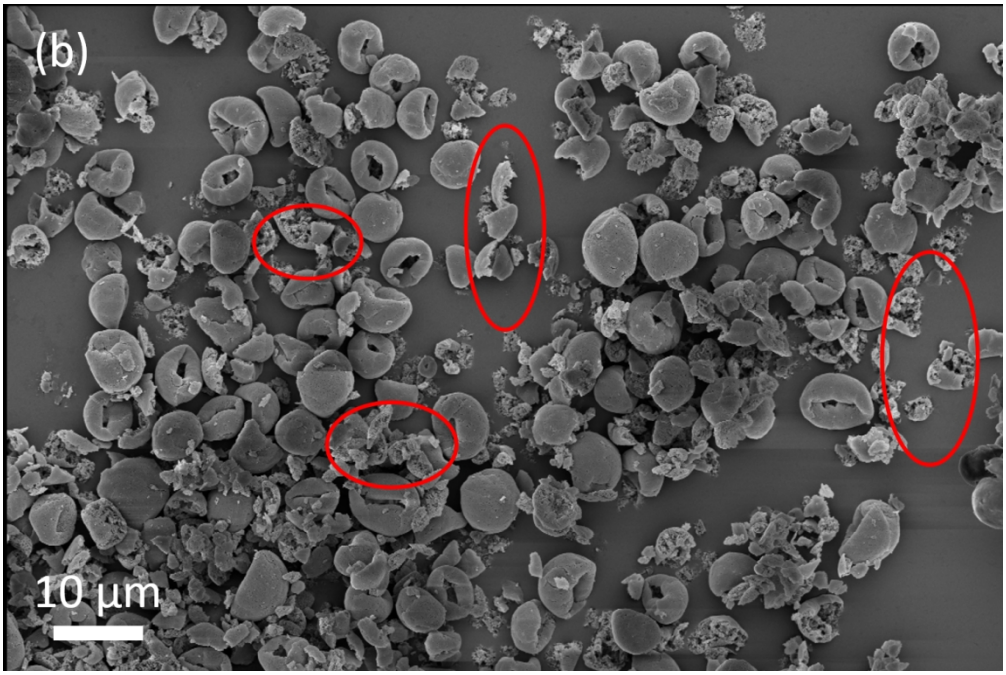
(b)
10 µm